Image-based analysis of weathered slag for calculation of transport properties and passive carbon capture

Faisal W. K. Khudhur [1]*, Alice Macente[1, 2], John M. MacDonald [1], Luke Daly [1,3,4]

[1] School of Geographical and Earth Sciences, University of Glasgow, Glasgow G12 8QQ, UK

[2] Department of Civil and Environmental Engineering, University of Strathclyde, Glasgow, G1 1XJ

[3] Centre for Microscopy and Microanalysis, University of Sydney, Sydney, 2006 NSW, Australia

[4] Department of Materials, University of Oxford, Oxford, OX1 3PH, UK

*Corresponding author: f.khudhur.1@research.gla.ac.uk

Abstract

Weathering of silicate-rich industrial wastes such as slag can reduce emissions from the steelmaking industry. During slag weathering, different minerals spontaneously react with atmospheric CO_2 to produce calcite. Here, we evaluate the CO_2 uptake during slag weathering using image-based analysis. The analysis was applied on an X-ray Computed Tomography dataset of a slag sample associated with the former Ravenscraig steelworks in Lanarkshire, Scotland. The element~~s~~ distribution of the sample was studied using scanning electron microscopy (SEM), coupled with energy dispersive spectroscopy (EDS). Two advanced image segmentation methods, namely trainable WEKA segmentation in the Fiji distribution of ImageJ and watershed segmentation in Avizo ® 9.3.0, were used to segment the XCT images into matrix, pore space, calcite and other precipitates. Both methods yielded similar volume fractions of the segmented classes. However, WEKA segmentation performed better in segmenting smaller pores, while watershed segmentation was superior in overcoming the partial volume effect presented in the XCT data. We estimate that CO_2

has been captured in the studied sample with an uptake between 20 and 17 kg CO_2/1000 kg slag for TWS and WS, respectively, through calcite precipitation.

Keywords

X-ray computed microtomography; EDS analysis; Image processing; Carbon capture; slag.

1. Introduction

Silicate weathering is a key mechanism by which nature controls the concentration of CO_2 in the atmosphere (Berner et al., 1983; Schuiling and Krijgsman, 2006). Silicate weathering includes the reaction of calcium and magnesium silicates with CO_2 to produce carbonate minerals, resulting in an estimated global natural carbon uptake rate of $1x10^{-3}$-$2.8x10^{-3}$ kg C m^{-2} y^{-1} (Amiotte Suchet et al., 2003; Gaillardet et al., 1999; Huh, 2003; Oskierski et al., 2013). Many studies investigated using different silicate rocks in negative emission technologies, and they showed that different sources, such as wastes from mining and steelmaking industries, have carbon uptake rates that are orders of magnitude larger than the corresponding natural values (Kelemen et al., 2020; Khudhur et al., 2022; Renforth et al., 2015; Zevenhoven and Kavaliauskaite, 2004). Using silicate-rich alkaline wastes like ironmaking and steelmaking slag to capture CO_2 is particularly attractive since these wastes are produced in large quantities ($7x10^{12}$-$1.7\ 10^{13}$ kg y^{-1}) with an annual carbon capture potential of $3.32x10^{11}$ kg C (Renforth et al., 2011). Slag is produced at different stages of ironmaking and steelmaking. Depending on the production method, ore composition and waste management practice, slag may be composed of several minerals such as larnite (Ca_2SiO_4), gehlenite ($Ca_2Al_2SiO_7$), åkermanite ($Ca_2MgSi_2O_7$), wustite (FeO) and other sulfur-containing minerals (Chukwuma et al., 2021; Scott et al., 1986). Ca and Mg minerals are added during ironmaking and steelmaking to remove the silicates that are present in the ore, resulting in producing slag that is rich in calcium silicates (Ghosh and Chatterjee, 2013). To reduce the environmental footprint of the steel industry, slag has been incorporated in several industries, such as cement production and road construction, resulting in high utilization of slag in Japan and the EU, with only <15% of the produced slag being disposed of. However, in other countries like

China, which produces ~50% of the world's crude steel, the utilization rate is low, resulting in over 70% of slag being sent for disposal (Guo et al., 2018).

Slag contains high concentrations of alkaline earth metal oxides which hydrate to produce hydroxides, which in turn generate alkalinity (Gomes et al., 2016). Such alkaline environments promote the ingassing and hydroxylation of atmospheric CO_2 in water. When CO_2 and water are in contact, equilibrium is established according to the following equations (Archer, 2007):

$$CO_2 + H_2O \rightarrow H_2CO_3 \leftrightarrow HCO_3^- + H^+ \quad (1)$$

$$HCO_3^- \leftrightarrow H^+ + CO_3^{2-} \quad (2)$$

As H^+ is generated, it results in dissolving silicates as shown in equation 3 (Daval et al., 2009; Yadav and Mehra, 2017):

$$M_xSi_yO_{x+2y-t}(OH)_{2t} + 2xH^+ \leftrightarrow xM^{2+} + ySiO_2 + (x+t)H_2O \quad (3)$$

Then, carbon sequestration occurs as a result of carbonates precipitation as illustrated in equation 4 and 5

$$xM^{2+} + xCO_3^{2-} \leftrightarrow xMCO_3 \quad (4)$$

Or

$$xM^{2+} + 2xHCO_3^- \leftrightarrow xMCO_3 + xCO_2 + xH_2O \quad (5)$$

The dissolution of silicates (equation 3) has been identified as the rate-limiting step, as silicate minerals contain several strong Si-O bonds that are difficult to break, resulting in nonstoichiometric dissolution of minerals that leave a Si-rich layer, as shown in Khudhur et al. (2022) and the referneces therein). This reaction can also be hindered due to carbonate precipitation that prevents further dissolution of silicates (Power et al., 2013).

Carbon sequestration during slag weathering has been documented in several studies. For example, Mayes et al. (2018) investigated the carbonation of a 1.6×10^7

m^3 slag heap located near Newcastle (UK), and they demonstrated that between $2.8x10^5$ and $2.9x10^6$ kg CO_2 has been captured within the slag heap since 1980. However, less than 3% of the CO_2 sequestration potential of the slag heap was passively utilized due to the emplacement conditions of the legacy slag, which hinder the interaction between reactive minerals and atmospheric CO_2 (Pullin et al., 2019).

Quantifying the amount of captured CO_2 can be done through conventional methods such as thermogravimetric analysis (TGA) or total inorganic carbon (TIC). However, these methods are destructive and result in loss of information related to pore size distribution, pore connectivity and internal reactive surface area. To fully understand the potential of passive CO_2 capture within slag deposits, non-destructive characterization of the porosity of slag and quantification of the captured CO_2 is required. This may be achieved by using X-ray Computed Tomography (XCT), a technique that has been widely used to study rock microstructure and mineralogy (e.g., Baker et al., 2012; Hua et al., 2021; Ketcham and Carlson, 2001; Singh et al., 2019; Wildenschild and Sheppard, 2013). An XCT dataset yields 2-dimensional cross-sections that are stacked to produce a three-dimensional rendering of the sample. This is particularly useful in different analyses, such as calculating porosity (e.g., Hyväluoma et al., 2012), visualizing minerals distribution (e.g., Garfi et al., 2020), understanding reaction mechanisms in heterogeneous rocks (e. g., Al-Khulaifi et al., 2017) and analyzing multiphase flow in rocks (e.g., Andrew et al., 2015).

The analysis of the XCT dataset is performed using image processing software. Software packages provide different methods for image segmentation, a process that enables image classification, according to specific criteria (e.g., image intensity), into discrete regions (Cheng et al., 2001; Sengur et al., 2019). Global segmentation methods, which depend on histogram evaluation and ignore pixel spatial distribution,

may give inaccurate results in segmenting low contrast samples (van Eijnatten et al., 2018). This is because an image histogram represents the grey level values distribution of pixels, and the grey level of a particular pixel in an XCT image depends on its X-ray attenuation coefficient, which is a function of the density, atomic number and X-ray energy, amongst other things (Baker et al., 2012). Consequently, pixels belonging to different phases having similar X-ray attenuation coefficients may overlap (Deboodt et al., 2021; Schlüter et al., 2014; Wildenschild and Sheppard, 2013). Additionally, limited scan resolution causes blurring at phase boundaries, resulting in intermediate grey level values that resemble other phases that are present in the studied volume. Therefore, machine learning-based methods and local segmentation methods (which depend on some neighborhood statistics to compensate for local intensity variation) have been developed to tackle challenging segmentation problems. Schlüter et al. (2014) summarized different approaches to image segmentation and concluded that these approaches experience different degrees of success depending on the nature of the studied sample. When studying XCT images of slag samples, image segmentation becomes challenging since slag is composed of minerals that have similar X-ray attenuation coefficients (Hanna and Ketcham, 2017; Reddy et al., 2019; Ter Teo et al., 2016). Consequently, the analysis of slag XCT images requires prior evaluation to define the advantages of different image processing pipelines.

In this work, we apply two robust image processing methods, namely, the machine learning-based Trainable WEKA Segmentation (TWS) in the Fiji distribution of ImageJ (Schindelin et al., 2012) and Watershed Segmentation (WS) in Avizo ® 9.3.0 (http://www.fei.com/software/avizo3d/), to analyze the XCT images of a legacy slag sample associated with the former Ravenscraig Steelworks in Lanarkshire (Scotland), and to compare the quality and reliability of the extracted information.

Results from both methods were compared to gain insights into the sensitivity of calculated properties to the processing pipeline. As TWS and WS require prior knowledge of the distribution of different elements within the studied sample, we used scanning electron microscopy (SEM) coupled with energy-dispersive X-ray spectroscopy (EDS) to identify features that can be used as training pixel and seed points in TWS and WS, respectively. Results of TWS and WS were used to study slag properties and to quantify passive CO_2 uptake.

2. Materials and Methods

2.1. Study Site

The slag sample was collected from Ravenscraig slag heap (55º 47' 21'' N, 3º 56' 25'' W) located in Lanarkshire (Scotland) where steelworks were active from 1957 to 1992 (Culture North Lanarkshire Museums, n.d.). The sample was collected from the surface of the heap, and it was cut into a small cube with a length of ~1 cm on each side using a water-cooled diamond saw to be studied to a high resolution using XCT and SEM-EDS.

2.2. XCT Analysis

In this work, we used the Nikon XT H320 LC X-ray computed tomography system of the Civil and Environmental Engineering department at the University of Strathclyde. System settings are summarized in Table 1. During XCT acquisition, the sample was mounted on a rotational stage, and 3141 X-ray 2D projections were collected over a 360° rotation, and were then mathematically converted to a stack of 2D reconstructed slices using the Nikon proprietary software through a mathematical operation known as filtered back-projection (Ketcham and Carlson, 2001). During reconstruction, data are converted into 16-bit grey scale images, where the intensity of grey is proportional to their attenuation coefficient: bright areas have higher attenuation values (e.g., oxides), whereas dark areas have low attenuation values (e.g., pores). The reconstructed images were then imported into different image processing software, to allow for 3D visualization and further analysis.

2.3. SEM Analysis

The sample that had been scanned by XCT was dissected using the diamond saw and mounted into a resin/hardener mixture so that it can be analyzed with the

SEM-EDS. The sample was ~~grinded~~ ground and then mechanically polished using a glycol suspension of 1-µm aluminum spheres for 5 minutes followed by a glycol suspension of 0.3-µm aluminum spheres for another 5 minutes. The final polishing step was carried out in a colloidal silica suspension for 4 hours.

The polished sample was sputter coated with a 20 nm conductive carbon layer. Then, sample imaging was conducted using a Zeiss Sigma VP Field-Emission Gun SEM (VP-FEG-SEM) equipped with X-Max 80 mm^2 silicon drift X-ray detector (Oxford Instrument), based in the ISAAC facility at the University of Glasgow (system settings are summarized in Table 1). Backscattered electron (BSE) images and EDS signals were acquired across the entire sample surface and were analyzed with Oxford Instrument AZtec ® 4.3 and AZtec ® Flex software.

2.4. Conventional Analysis

To provide better understanding of the studied slag sample, offcut material was pulverized using mortar and pestle until it passed through a 45 µm sieve, and it was analyzed using thermogravimetric analysis (TGA) and X-ray diffraction analysis (XRD). The former provides an estimate regarding the $CaCO_3$ content of the studied material while the latter provides an idea about the mineral composition of the studied sample. TGA was performed on TGA 5500 (TA Instruments, USA) under N_2 atmosphere, with a heating rate of 10 ºC/min, while powder XRD patterns were collected using a Rigaku MiniFlex 6G equipped with a Cu sealed tube (Ka1 and Ka2 wavelengths - 1.5406 and 1.5444 Å respectively). Data collection and analysis were performed using Rigaku SmartLab Studio II software (Rigaku Corporation, 2022).

2.5. Image Processing

The reconstructed XCT volume was cropped to remove external space and to remove noise and artifacts near sharp edges, resulting in a studied volume of 11.41 x 11.98 x 5.97 mm^3. In Avizo ® 9.3.0, The *slice* module was used to find the cross-section within the studied volume that is well-aligned with the collected BSE/EDS images (Supplementary Information S1). Such alignment is essential in finding pixels that can be used as training pixels and seed points in TWS and WS, respectively, and to identify features that are below the XCT resolution. Since XCT and BSE images rely on the composition of the studied sample, the coefficient of correlation was used as a metric for alignment quality, as explained in a previous study (Latham et al., 2008). From there, two different image processing pipelines were used: the machine learning-based TWS in Fiji, and the WS in Avizo ® 9.3.0 (Fig.1).

Machine learning-based segmentation involves training a computer to recognize patterns in the same (or improved) manner that a human operator recognizes them. In the TWS plugin of Fiji, the operator manually labels pixels and assigns them to different classes (Arganda-Carreras et al., 2016). These “training pixels” are then used to extract different features needed to classify the entire dataset. TWS has different training features (e.g. image filters) that can be selected as per different training needs, such as noise reduction (e.g., gaussian blur), detection of objects boundaries (e.g., sobel), extraction of information related to image texture and localization of membrane-like structures (e.g., structure) (Arganda-Carreras et al., 2017; Hall et al., 2009). TWS has been successfully used in segmenting geological samples without requiring prefiltering steps (Garfi et al., 2020; Purswani et al., 2020). Therefore, we used the TWS to segment XCT images of the slag sample, and we used

the default classifier of TWS, which is the fast random forest that uses 200 trees, constructed while considering 2 random features. It should be noted that based on the complexity of the mathematical operations embedded within each feature, the combination of the selected features can result in long processing time (up to 10 hours). Initially, we created 14 different training files that contain different training features (Supplementary Information S2) to investigate how feature selection affected calculation time and segmentation quality. A subset of the sample (a stack of 51 images) was segmented using these training features (while using the same training pixels). Evaluation of the different training files was based on visual inspection of the results, the processing time (including features extraction time and classifying time), and the complexity of the segmentation, which is reflected by the number of features. Additionally, the prediction quality of the machine learning classifier was considered through a comparison of the out-of-bag error that TWS reports for each segmentation file (Supplementary Information S2). The classifiers with the lowest out-of-bag error are the most suited for the classification. These criteria were used to find the combination of the features that was used to segment the entire studied volume in a reasonable time (less than 2 hours).

Commented [Jfm1]: Supplementary Information

Commented [Jfm2]: Supplementary Information

In the second pipeline, watershed segmentation (WS) in Avizo ® 9.3.0 was used to segment the same sample. WS has been widely used in segmenting geological samples and cementitious composites (Berg et al., 2016; Lee et al., 2009; Rücker et al., 2015), and it succeeded in segmenting low contrast samples (Deboodt et al., 2021). The watershed concept was first introduced by Digabel and Lantuejoul (1978) and was later improved by Beucher and Lantuéjoul (1979) who used it for contours detection. A major improvement to the watershed algorithm was introduced by Vincent and Soille (1991) who provided an algorithm that is orders of magnitude

faster than the previous version (Preim and Botha, 2014). Several watershed-based algorithms have been developed since then as summarized by Roerdink and Meijster (2000). The WS can be thought of as a conversion of an image to a topographical landscape, where the height of each point reflects the pixel value at that point (Deboodt et al., 2021; Leu et al., 2014). This segmentation is performed by first identifying how many phases need to be segmented. Then, boundaries between different classes are identified by finding the lines of highest gradients via a small cubic kernel or an edge detection filter, assuming that boundaries between different classes are distinguished by a high gradient. Then, seed points for distinguishing different classes are identified by thresholding (Deboodt et al., 2021). A watershed algorithm is then applied to grow the seeds until watershed lines are met, analogous to how rainwater fills valleys until it meets (but does not mix) the watershed lines. Points on the watershed lines are assigned according to their neighborhood (Schlüter et al., 2014).

The WS aims to overcome the partial volume effect, a common problem caused by resolution limitation that makes voxels at transitional regions blurry and prone to misclassification (Schlüter et al., 2014). The image stack was imported to Avizo ® 9.3.0 and then the non-local means denoising filter (NLMD) with search window=20 pixels, local neighborhood=5 pixels and similarity value=0.4 was applied. This filter was selected as it removes image noise without significant blurring to edges, and it was successfully used in several studies for noise removal (Garfi et al., 2020; Schlüter et al., 2014; Shah et al., 2016). The *watershed wizard* was used to define watershed lines and seed points for the different phases.

After segmentation of the entire dataset, the *remove island* filter was used to discard features that are less than 27 voxels which, due to limitations in resolution,

can be misclassified, as described elsewhere (Oluwadebi et al., 2019). The *volume fraction* module in Avizo ® 9.3.0 was used to calculate the volume fractions of the segmented phases. Error bars were calculated by finding the change of volume fractions after applying morphological dilation and erosion operations to the segmentation results, with a cubic structural element, a 6-pixel neighborhood and a half-kernel size of 1 pixel to the segmentation results. Using morphological operations in error estimation is arguably conservative, and has been used for this purpose in previous research (Fusseis et al., 2012; Macente et al., 2018, 2017). To visualize the connected pore space, the *connected components* module in Avizo ® was used to show the voxels that have at least one common face, as described by Sarkar and Siddiqua (2016). Finally, a *separate object* module, with a marker extent =1 and neighborhood=26, was used to separate the pores individually based on their pore throats. A *label analysis* module was used on the separated pores to calculate equivalent pore diameter and mean equivalent diameter. The studied volume size is 1.36 GB and all processing was performed on a desktop with Intel ® Xeon ® CPU with a clock speed of 3.5 GHz and 128 GB RAM.

3. Results and Discussion

3.1. Microstructural and textural characterization

Fig. 2 presents different results of the XCT analysis process. Fig. 2a represents a 2D radiograph of the scanned sample, whereas Fig. 2b and 2c represent an XY cross-sectional slice of the sample after reconstruction before and after cropping, respectively. In these images, dark and bright regions refer to void space and slag matrix, respectively. Areas that have intermediate grey level values, such as those marked in Fig. 2e represent calcite and other precipitates. Fig. 2d shows the intensity frequency histogram of the studied sample, demonstrating a bimodal distribution,

where the low and high peaks represent the void space and the matrix, respectively. Due to the low abundance of calcite and other precipitates and due to the similarity of X-ray attenuation coefficients of the former to other minerals in the slag, there seems to be no distinctive peaks for calcite and other precipitates, resulting in a complex segmentation procedure. Therefore, BSE and EDS results (Fig. 3 and Fig. 4) were used to identify the chemistry of different regions in the acquired XCT data. To illustrate, in Fig. 3b the region depicted by spectrum A (Fig. 3c) is rich in Si, while spectrum B shows enrichment in Ca and depletion in Si content, suggesting conversion of calcium silicates to carbonate, in agreement with equations (1) through (5). Other regions have elevated contents of elements such as sulfur (spectrum C in Fig. 3b, c) reflecting other components in the slag. Fig. 4 shows EDS maps for Si, Ca, S, C and O, indicating that the studied sample is generally dominated by Ca-silicates rich phases, with minor amounts of other compounds.

Fig. 2 hereabout.

3.2. TWS Features Selection

Representative segmentation results of different TWS training sets are portrayed in the Supplementary Information (S2). As the number of features increased, segmentation time also increased (Supplementary Fig. S4), although no specific trend (e.g., linear or exponential) was observed. Default training settings, represented by training set 1, require 76 training features and it took longer time compared to other training settings (Supplementary Table S1). The selection of training features affects the volume fraction of the classified phases (Supplementary Fig. S5), and segmentation errors were observed to occur near the boundaries between void space and other phases, analogous to misclassification observed in a related study where similar image processing pipelines were used (Garfi et al., 2020). These errors result in segmenting small pores as precipitates and classifying the borders between pores and matrix as calcite.

To identify the best training features to be used in segmenting the entire dataset (i.e., the 576-image stack), segmentation time and quality were used as selection criteria. The former was qualitatively predicted based on the number of features (i.e., higher number of features results in longer segmentation time), while the latter was based on comparing calcite distribution with SEM data and based on misclassification that occurs at boundaries and edges due to the partial volume effect, and by calculating the out-of-bag error. Such misclassification appears at pore boundaries as outer rims in regions where SEM analysis shows no calcite had formed. Inspection of Supplementary Fig. S6 reveals that training sets 7 and 13 have a relatively smaller partial volume effect (i.e., smaller misclassification of contact area between pores and matrix as calcite) compared to the rest of the training methods. Additionally, Supplementary Fig. S5 portrays that training sets 7 and 13 predict volume fractions

Commented [Jfm3]: Supplementary Information

Commented [Jfm4]: Supplementary Information

Commented [Jfm5]: Supplementary Information

Commented [Jfm6]: Supplementary Information

Commented [Jfm7]: Supplementary Information

Commented [Jfm8]: Supplementary Information

that are close to the average and median values (calculated to be 4.7% and 4.8%, respectively) of the predicted volume fraction of calcite by the 14 training combinations, and both have close out-of-bag error of 0.351% and 0.276%, respectively. As training set 13 has a smaller number of features, the 576-image stack was trained using the same features of training set 13 (gaussian blur, Sobel, structure).

3.3. Segmentation Results

Results from both segmentation methods for representative cross-sections are portrayed in Fig. 5. Some differences can be observed between the two pipelines. For example, it is evident from Fig. 5 (part A) that TWS was inferior to WS at boundaries since the former misclassified pixels located at boundaries between the matrix and precipitate or the matrix and the pore space as calcite. On the other hand, TWS performed better in segmenting smaller pores (Fig. 5 part B) due to the lack of pre-filtering, since smaller pores may be blurred as a result of filtering, causing them to be misclassified as observed in similar studies (Garfi et al., 2020; Shah et al., 2016). Segmentation results in Fig. 5 reveal the complexity of the studied sample. That is, calcite precipitated in sporadic manner, and in the linings of pores and intertwined with other precipitates. This complexity is a consequence of slag composition which includes several minerals that have X-ray attenuation coefficients with similar values to calcite (Hanna and Ketcham, 2017). Additionally, calcite is produced from several reactions between CO_2, water, and slag minerals that are difficult to identify, even with SEM imaging as shown in Fig. 3d. Both processing pipelines showed that the matrix layer contained dispersed precipitate regions. These regions may originate due to a redistribution of transition elements within alkaline wastes because of weathering and precipitation (Hamilton et al., 2018). Slag heterogeneity increases further during

weathering due to interaction with water, which results in formation of complex aluminosilicate layer (You et al., 2011).

3.4. Volume fractions of segmented phases

Fig. 6 displays 3D volume renderings of segmented calcite and other non-calcite precipitates as calculated from both methods, while Fig. 7 summarizes calculated volume fractions of pores, slag matrix, calcite and non-calcite precipitates, displaying good agreement between both pipelines. Calcite content is particularly important to this study since it can be used to calculate the carbon capture potential of slag. According to the implemented segmentation, calcite content was calculated to be 3.1% (TWS) and 2.7% (WS). Taking the bulk density of slag sample to be 1.927 g/cm^3 (measured in our laboratory) and the density of calcite to be 2.71 g/cm^3 (DeFoe and Compton, 1925), we calculated that the carbon capture storage potential of this slag is 20 kg/1000 kg slag (calculated per CO_2-free slag) and 17 kg/1000 kg for TWS and WS, respectively. Both values are below the value of 29 kg CO_2/ 1000 kg slag that was calculated based on TGA analysis (Supplementary Information S5). TGA analysis can overestimate the CO_2 content since other slag minerals such as hydrated silicates decompose at the temperature range in which calcite decomposes (Pan et al., 2016). Additionally, calcite can precipitate in smaller pores with diameters of 1 μm, making it undetectable with the resolution of both XCT and SEM images of this study, (Arandigoyen et al., 2006). When applying the erosion and dilation operation for error bar estimation (Fig. 7), the CO_2 uptake ranges will be 4.42 to 44.6 kg CO_2/ 1000 kg slag and 5.6-34 kg CO_2/ 1000 kg slag for TWS and WS, respectively, indicating that the CO_2 uptake value based on TGA falls within the error bars range calculated based on erosion and dilation operations. Generally, applying the erosion and dilation

Commented [Jfm9]: Supplementary Information

operations results in larger error bars range when compared to other methods of error estimation such as changing the training pixels and the segmentation parameters for the TWS and WS, respectively (Supplementary Information S7).

Commented [Jfm10]: Supplementary Information

While the estimated uptake of CO_2 in this study is only a fraction of ex-situ carbonation which ranges from 107 to 283 kg CO_2 /1000 kg slag (Chang et al., 2011), it reflects CO_2 uptake from the atmosphere achievable at no cost, compared to that of ex-situ carbonation that requires energy-intensive operations, such as crushing of slag to the microscale and performing the reaction at elevated temperature and pressure that can reach 160 °C and 4.8 MPa, respectively (Chang et al., 2011). Crouzet et al. (2017) reported a passive CO_2 uptake equal to 63 kg CO_2/1000 kg slag (based on TGA analysis) in a slag heap at a French production site. Our calculated value of CO_2 uptake has the same order of magnitude of the value reported by Crouzet et al. (2017) despite being lower. In addition to the differences in the measuring methods, several factors justify the observed difference. For example, slag properties, such as chemical composition and size distribution, vary based on the processing routes and the properties of the starting material (Proctor et al., 2000; Sanna et al., 2012). Additionally, carbonate precipitation in environments associated with alkaline wastes varies across sites according to different factors such as rain received and region topography (Mayes et al., 2018; Wilson et al., 2009). Carbon capture in passively managed environments is hindered by CO_2 supply and slag size distribution (Pullin et al., 2019). It should be noted that carbonation can also be inhibited as a result of calcite precipitation, which results in clogging of pores and prevention of further carbonation (see Section 3.5). Additionally, exposure to water can result in silica gel polymerization

which in turn results in the formation of a barrier that inhibits further carbonation (Assima et al., 2012; Khudhur et al., 2022). Despite this, we show that passive carbonation indeed occurred at the Ravenscraig site, and that non-destructive image-based analysis can be used to estimate carbon capture potential.

3.5. Pore space analysis

Table 2 summarizes the total porosity, surface area and mean equivalent diameter of the studied sample, as calculated from both pipelines. While TWS and WS calculated similar total porosity, other complex transport properties such as pore surface area and equivalent diameters were more sensitive to the processing pipeline as shown in Table 2 and Fig. 8. Garfi et al. (2020) noted that the sensitivity of a property estimate to the processing pipeline increases with the increased complexity of the definition of that property, and they showed that the percentage error between TWS and WS estimation of porosity for Berea sandstone was 26%, while it was 83% for the estimation of single-phase permeability. Porosity estimations through XCT is usually underestimated (Boone et al., 2014). This underestimation increases as the resolution is decreased, causing pores to blur or completely disappear (Shah et al., 2016). This can be observed when comparing the XCT slice with the higher resolution BSE image shown in Supplementary Fig. S1.

Commented [Jfm11]: Supplementary Information

Pore connectivity is an important feature that affects materials reactivity since the surface of the pore represents the area at which dissolution, leaching, and precipitation occur. In the study of reactions in porous media, it is known that reaction behavior in such media is different from the bulk phase reaction and that precipitation is affected by the pores size (Turner et al., 2002; Zachara et al., 2016). While Putnis

and Mauthe (2001) demonstrated that precipitation of salts within sandstone is preferential at pores with diameters of 10-40 μm, Arandigoyen et al. (2006) demonstrated that calcite precipitation proceeds preferentially in smaller pores with diameters less than 1 μm, although this could not be observed in the current study due to the limited resolution of both imaging techniques. In Fig. 9 we present the pore space as segmented by TWS and WS. Fig. 9c, d shows the largest five connected pore clusters. If we account for the pores and precipitates together, (i.e., before any precipitation occurred), Fig.9e and Fig.9f show that the connected component profile changes significantly, demonstrating that the area that is rich in calcite had been part of a larger connected pore space prior to precipitation. As precipitation occurred, the connected space changed and consequently resulted in a reduction of fluid accessibility to the reactive site within the slag. The study of (Crouzet et al., 2017) showed that passive carbonation occurred at an early stage after slag production (i.e., slag aged in weeks had CO_2 content of 5.9 wt% while slag aged in years had CO_2 content of 6.3 wt%), possibly indicating reduced access of reactive components after precipitation which slowed the carbonation process.

4. Conclusion

While conventional tools such as TGA and TIC are successfully used to study CO_2 uptake within slag, image-based analysis gives new insights regarding pore networks and the spatial distribution of minerals within the studied sample. In this work, we used two advanced image processing pipelines to segment XCT images of a slag sample into four classes: matrix, pores, calcite and non-calcite precipitates. Namely, we used the machine learning-based trainable WEKA segmentation in the first pipeline, while we used nonlocal means denoising filter followed by watershed

segmentation in the second pipeline. Both methods come with advantages and drawbacks. The advantage of the TWS plugin of Fiji is that it is freely available and provides users with strong machine learning capabilities to segment images based on many features in addition to their grey level values. However, selecting the right combination of features and training pixels may be challenging and performing the segmentation may require a long time (up to 10 hours) and computing power that is not always available. The WS segmentation requires much less time to be performed but requires filtering that may blur smaller pores and consequently introducing additional errors. Both methods provided similar volume fractions. This was not the case with the pores equivalent diameters as TWS showed a larger number of smaller pores. This was attributed to the higher success of TWS in segmenting pores with volumes.

Considering that TWS quantified similar volume fractions to WS, but it has a higher success in segmenting smaller pore and pore throats, and that it is a freely available tool, this study recommends using it in image-based analysis of slag samples. The proposed workflow demonstrates that the low slag carbonation is attributed to the low exposure of reactive surface area to CO_2, in addition to low atmospheric CO_2 and low ambient temperature.

5. Acknowledgement

Faisal W. K. Khudhur acknowledges support from the University of Glasgow Lord Kelvin/Adam Smith PhD scholarship. Dr. Mark Wildman, Dr. Connor Brolly and Dr. Sammy Griffin of the School of Earth Sciences at the University of Glasgow are acknowledged for assisting in sample preparation and analysis. Dr. Liene Spruženiece of the Imaging Spectroscopy and Analysis Centre at the University of Glasgow and Peter Chung are acknowledged for supporting SEM data acquisition and analysis. Dr.

Claire Wilson and Mr Andrew Monaghan of the School of Chemistry at the University of Glasgow are acknowledged for supporting the XRD and TGA analysis. Three reviewers are acknowledged for their remarks that greatly improved this manuscript. Finally, the authors declare no known competing interest.

6. References

Al-Khulaifi, Y., Lin, Q., Blunt, M.J., Bijeljic, B., 2017. Reaction Rates in Chemically Heterogeneous Rock: Coupled Impact of Structure and Flow Properties Studied by X-ray Microtomography. Environ. Sci. Technol. 51, 4108–4116. https://doi.org/10.1021/ACS.EST.6B06224

Amiotte Suchet, P., Probst, J.-L., Ludwig, W., 2003. Worldwide distribution of continental rock lithology: Implications for the atmospheric/soil CO 2 uptake by continental weathering and alkalinity river transport to the oceans. Global Biogeochem. Cycles 17. https://doi.org/10.1029/2002GB001891

Andrew, M., Menke, H., Blunt, M.J., Bijeljic, B., 2015. The Imaging of Dynamic Multiphase Fluid Flow Using Synchrotron-Based X-ray Microtomography at Reservoir Conditions. Transp. Porous Media 2015 1101 110, 1–24. https://doi.org/10.1007/S11242-015-0553-2

Arandigoyen, M., Bicer-Simsir, B., Alvarez, J.I., Lange, D.A., 2006. Variation of microstructure with carbonation in lime and blended pastes. Appl. Surf. Sci. 252, 7562–7571. https://doi.org/10.1016/J.APSUSC.2005.09.007

Archer, D., 2007. Global Warming: Understanding the Forecast, 1st ed. Blackwell Publishing.

Arganda-Carreras, I., Kaynig, V., Rueden, C., Eliceiri, K.W., Schindelin, J., Cardona,

A., Seung, H.S., 2017. Trainable Weka Segmentation: A machine learning tool for microscopy pixel classification. Bioinformatics 33, 2424–2426. https://doi.org/10.1093/bioinformatics/btx180

Arganda-Carreras, I., Kaynig, V., Rueden, C., Schindelin, J., Cardona, A., Seung, H.S., 2016. Trainable_Segmentation: Release v3.1.2. https://doi.org/10.5281/ZENODO.59290

Assima, G.P., Larachi, F., Beaudoin, G., Molson, J., 2012. CO2 Sequestration in Chrysotile Mining Residues—Implication of Watering and Passivation under Environmental Conditions. Ind. Eng. Chem. Res. 51, 8726–8734. https://doi.org/10.1021/IE202693Q

Baker, D.R., Mancini, L., Polacci, M., Higgins, M.D., Gualda, G.A.R., Hill, R.J., Rivers, M.L., 2012. An introduction to the application of X-ray microtomography to the three-dimensional study of igneous rocks. Lithos 148, 262–276. https://doi.org/10.1016/j.lithos.2012.06.008

Berg, S., Rücker, M., Ott, H., Georgiadis, A., van der Linde, H., Enzmann, F., Kersten, M., Armstrong, R.T., de With, S., Becker, J., Wiegmann, A., 2016. Connected pathway relative permeability from pore-scale imaging of imbibition. Adv. Water Resour. 90, 24–35. https://doi.org/10.1016/J.ADVWATRES.2016.01.010

Berner, R.A., Lasaga, A.C., Garrels, R.M., 1983. The carbonate-silicate geochemical cycle and its effect on atmospheric carbon dioxide over the past 100 million years. Am. J. Sci. 283, 641–683. https://doi.org/10.2475/ajs.283.7.641

Beucher, S., Lantuéjoul, C., 1979. Use of Watersheds in Contour Detection, in: International Workshop on Image Processing, Real-Time Edge and Motion Detection.

Boone, M.A., Nielsen, P., De Kock, T., Boone, M.N., Quaghebeur, M., Cnudde, V., 2014. Monitoring of Stainless-Steel Slag Carbonation Using X-ray Computed Microtomography. Environ. Sci. Technol. 48, 674–680. https://doi.org/10.1021/es402767q

Chang, E.E., Pan, S.Y., Chen, Y.H., Chu, H.W., Wang, C.F., Chiang, P.C., 2011. CO2 sequestration by carbonation of steelmaking slags in an autoclave reactor. J. Hazard. Mater. 195, 107–114. https://doi.org/10.1016/j.jhazmat.2011.08.006

Cheng, H.D., Jiang, X.H., Sun, Y., Wang, J., 2001. Color image segmentation: advances and prospects. Pattern Recognit. 34, 2259–2281. https://doi.org/10.1016/S0031-3203(00)00149-7

Chukwuma, J.S., Pullin, H., Renforth, P., 2021. Assessing the carbon capture capacity of South Wales' legacy iron and steel slag. Miner. Eng. 173, 107232. https://doi.org/10.1016/J.MINENG.2021.107232

Crouzet, C., Brunet, F., Montes-Hernandez, G., Recham, N., Findling, N., Ferrasse, J.H., Goffé, B., 2017. Hydrothermal valorization of steel slags-Part I: Coupled H2 production and CO2 mineral sequestration. Front. Energy Res. 5, 1–12. https://doi.org/10.3389/fenrg.2017.00029

Culture North Lanarkshire Museums, n.d. Ravenscraig & the Steel Industry in Lanarkshire [WWW Document]. URL https://www.culturenlmuseums.co.uk/story/ravenscraig-and-the-steel-industry-in-lanarkshire/ (accessed 6.24.21).

Daval, D., Martinez, I., Corvisier, J., Findling, N., Goffé, B., Guyot, F., 2009. Carbonation of Ca-bearing silicates, the case of wollastonite: Experimental investigations and kinetic modeling. Chem. Geol. 265, 63–78. https://doi.org/10.1016/J.CHEMGEO.2009.01.022

Deboodt, T., Wildenschild, D., Ideker, J.H., Burkan Isgor, O., 2021. Comparison of thresholding techniques for quantifying portland cement hydrates using synchrotron microtomography. Constr. Build. Mater. 266, 121109. https://doi.org/10.1016/j.conbuildmat.2020.121109

DeFoe, O.K., Compton, A.H., 1925. The Density of Rock Salt and Calcite. Phys. Rev. 25, 618–620. https://doi.org/10.1103/PhysRev.25.618

Digabel, H., Lantuejoul, C., 1978. Iterative Algorithms, in: Proceedings of the 2nd European Symposium Quantitative Analysis of Microstructures in Material Science, Biology and Medicine. pp. 85–89.

Fusseis, F., Schrank, C., Liu, J., Karrech, A., Llana-Fúnez, S., Xiao, X., Regenauer-Lieb, K., 2012. Pore formation during dehydration of a polycrystalline gypsum sample observed and quantified in a time-series synchrotron X-ray micro-tomography experiment. Solid Earth 3, 71–86. https://doi.org/10.5194/SE-3-71-2012

Gaillardet, J., Dupré, B., Louvat, P., Allègre, C.J., 1999. Global silicate weathering and CO2 consumption rates deduced from the chemistry of large rivers. Chem. Geol. 159, 3–30. https://doi.org/10.1016/S0009-2541(99)00031-5

Garfi, G., John, C.M., Berg, S., Krevor, S., 2020. The Sensitivity of Estimates of Multiphase Fluid and Solid Properties of Porous Rocks to Image Processing. Transp. Porous Media 131, 985–1005. https://doi.org/10.1007/s11242-019-01374-z

Ghosh, A., Chatterjee, A., 2013. Ironmaking and Steelmaking. PHI Learning Private Limited.

Gomes, H.I., Mayes, W.M., Rogerson, M., Stewart, D.I., Burked, I.T., 2016. Alkaline residues and the environment: A review of impacts, management practices and

opportunities. J. Clean. Prod. https://doi.org/10.1016/j.jclepro.2015.09.111

Guo, J., Bao, Y., Wang, M., 2018. Steel slag in China: Treatment, recycling, and management. Waste Manag. 78, 318–330. https://doi.org/10.1016/J.WASMAN.2018.04.045

Hall, M., Frank, E., Holmes, G., Pfahringer, B., Reutemann, P., Witten, I.H., 2009. The WEKA data mining software. ACM SIGKDD Explor. Newsl. 11, 10–18. https://doi.org/10.1145/1656274.1656278

Hamilton, J.L., Wilson, S.A., Morgan, B., Turvey, C.C., Paterson, D.J., Jowitt, S.M., McCutcheon, J., Southam, G., 2018. Fate of transition metals during passive carbonation of ultramafic mine tailings via air capture with potential for metal resource recovery. Int. J. Greenh. Gas Control 71, 155–167. https://doi.org/10.1016/j.ijggc.2018.02.008

Hanna, R.D., Ketcham, R.A., 2017. X-ray computed tomography of planetary materials: A primer and review of recent studies. Geochemistry 77, 547–572. https://doi.org/10.1016/J.CHEMER.2017.01.006

Hua, G., Wu, S., Jing, Z., Yu, X., Xu, K., Shi, W., Guan, M., 2021. Rock physical and chemical alterations during the in-situ interaction between fracturing fluid and Silurian organic-rich shales in China. J. Nat. Gas Sci. Eng. 94, 104075. https://doi.org/10.1016/j.jngse.2021.104075

Huh, Y., 2003. Chemical weathering and climate — a global experiment: A review. Geosci. J. 7, 277–288. https://doi.org/10.1007/BF02910294

Hyväluoma, J., Thapaliya, M., Alaraudanjoki, J., Sirén, T., Mattila, K., Timonen, J., Turtola, E., 2012. Using microtomography, image analysis and flow simulations to characterize soil surface seals. Comput. Geosci. 48, 93–101. https://doi.org/10.1016/j.cageo.2012.05.009

Kelemen, P.B., McQueen, N., Wilcox, J., Renforth, P., Dipple, G., Vankeuren, A.P., 2020. Engineered carbon mineralization in ultramafic rocks for CO2 removal from air: Review and new insights. Chem. Geol. 550, 119628. https://doi.org/10.1016/j.chemgeo.2020.119628

Ketcham, R.A., Carlson, W.D., 2001. Acquisition, optimization and interpretation of x-ray computed tomographic imagery: Applications to the geosciences. Comput. Geosci. 27, 381–400. https://doi.org/10.1016/S0098-3004(00)00116-3

Khudhur, F.W.K., MacDonald, J.M., Macente, A., Daly, L., 2022. The utilization of alkaline wastes in passive carbon capture and sequestration: Promises, challenges and environmental aspects. Sci. Total Environ. 823, 153553. https://doi.org/10.1016/J.SCITOTENV.2022.153553

Latham, S.J., Varslot, T., Sheppard, A., 2008. Automated registration for augmenting micro-CT 3D images. ANZIAM J. 50, 534. https://doi.org/10.21914/anziamj.v50i0.1389

Lee, B.Y., Kim, J.K., Kim, J.S., Kim, Y.Y., 2009. Quantitative evaluation technique of Polyvinyl Alcohol (PVA) fiber dispersion in engineered cementitious composites. Cem. Concr. Compos. 31, 408–417. https://doi.org/10.1016/J.CEMCONCOMP.2009.04.002

Leu, L., Berg, S., Enzmann, F., Armstrong, R.T., Kersten, M., 2014. Fast X-ray Micro-Tomography of Multiphase Flow in Berea Sandstone: A Sensitivity Study on Image Processing. Transp. Porous Media 105, 451–469. https://doi.org/10.1007/s11242-014-0378-4

Macente, A., Fusseis, F., Butler, I.B., Tudisco, E., Hall, S.A., Andò, E., 2018. 4D porosity evolution during pressure-solution of NaCl in the presence of phyllosilicates. Earth Planet. Sci. Lett. 502, 115–125.

https://doi.org/10.1016/j.epsl.2018.08.032

Macente, A., Fusseis, F., Menegon, L., Xianghui, X., John, T., 2017. The strain-dependent spatial evolution of garnet in a high-P ductile shear zone from the Western Gneiss Region (Norway): a synchrotron X-ray microtomography study. J. Metamorph. Geol. 35, 565–583. https://doi.org/10.1111/jmg.12245

Mayes, W.M., Riley, A.L., Gomes, H.I., Brabham, P., Hamlyn, J., Pullin, H., Renforth, P., 2018. Atmospheric CO 2 Sequestration in Iron and Steel Slag: Consett, County Durham, United Kingdom. Environ. Sci. Technol. 52, 7892–7900. https://doi.org/10.1021/acs.est.8b01883

Oluwadebi, A.G., Taylor, K.G., Ma, L., 2019. A case study on 3D characterisation of pore structure in a tight sandstone gas reservoir: The Collyhurst Sandstone, East Irish Sea Basin, northern England. J. Nat. Gas Sci. Eng. 68, 102917. https://doi.org/10.1016/J.JNGSE.2019.102917

Oskierski, H.C., Dlugogorski, B.Z., Jacobsen, G., 2013. Sequestration of atmospheric CO2 in chrysotile mine tailings of the Woodsreef Asbestos Mine, Australia: Quantitative mineralogy, isotopic fingerprinting and carbonation rates. Chem. Geol. 358, 156–169. https://doi.org/10.1016/j.chemgeo.2013.09.001

Pan, S.Y., Chang, E.E., Kim, H., Chen, Y.H., Chiang, P.C., 2016. Validating carbonation parameters of alkaline solid wastes via integrated thermal analyses: Principles and applications. J. Hazard. Mater. 307, 253–262. https://doi.org/10.1016/J.JHAZMAT.2015.12.065

Power, I.M., Harrison, A.L., Dipple, G.M., Wilson, S.A., Kelemen, P.B., Hitch, M., Southam, G., 2013. Carbon Mineralization: From Natural Analogues to Engineered Systems. Rev. Mineral. Geochemistry 77, 305–360. https://doi.org/10.2138/rmg.2013.77.9

Preim, B., Botha, C., 2014. Image Analysis for Medical Visualization, in: Visual Computing for Medicine. Morgan Kaufmann, pp. 111–175. https://doi.org/10.1016/B978-0-12-415873-3.00004-3

Proctor, D.M., Fehling, K.A., Shay, E.C., Wittenborn, J.L., Green, J.J., Avent, C., Bigham, R.D., Connolly, M., Lee, B., Shepker, T.O., Zak, M.A., 2000. Physical and chemical characteristics of blast furnace, basic oxygen furnace, and electric arc furnace steel industry slags. Environ. Sci. Technol. 34, 1576–1582. https://doi.org/10.1021/es9906002

Pullin, H., Bray, A.W., Burke, I.T., Muir, D.D., Sapsford, D.J., Mayes, W.M., Renforth, P., 2019. Atmospheric Carbon Capture Performance of Legacy Iron and Steel Waste. Environ. Sci. Technol. 53, 9502–9511. https://doi.org/10.1021/acs.est.9b01265

Purswani, P., Karpyn, Z.T., Enab, K., Xue, Y., Huang, X., 2020. Evaluation of image segmentation techniques for image-based rock property estimation. J. Pet. Sci. Eng. 195, 107890. https://doi.org/10.1016/j.petrol.2020.107890

Putnis, A., Mauthe, G., 2001. The effect of pore size on cementation in porous rocks. Geofluids 1, 37–41. https://doi.org/10.1046/j.1468-8123.2001.11001.x

Reddy, K.R., Chetri, J.K., Kumar, G., Grubb, D.G., 2019. Effect of basic oxygen furnace slag type on carbon dioxide sequestration from landfill gas emissions. Waste Manag. 85, 425–436. https://doi.org/10.1016/J.WASMAN.2019.01.013

Renforth, P., Pogge von Strandmann, P.A.E., Henderson, G.M., 2015. The dissolution of olivine added to soil: Implications for enhanced weathering. Appl. Geochemistry 61, 109–118. https://doi.org/10.1016/j.apgeochem.2015.05.016

Renforth, P., Washbourne, C.-L., Taylder, J., Manning, D.A.C., 2011. Silicate Production and Availability for Mineral Carbonation. Environ. Sci. Technol. 45,

2035–2041. https://doi.org/10.1021/es103241w

Rigaku Corporation, 2022, 2022. SmartLab Studio II [WWW Document]. URL https://www.rigaku.com/products/xrd/studio (accessed 3.24.22).

Roerdink, J.B.T.M., Meijster, A., 2000. The Watershed Transform: Definitions, Algorithms and Parallelization Strategies. Fundam. Informaticae 41, 187–228. https://doi.org/10.3233/FI-2000-411207

Rücker, M., Berg, S., Armstrong, R.T., Georgiadis, A., Ott, H., Schwing, A., Neiteler, R., Brussee, N., Makurat, A., Leu, L., Wolf, M., Khan, F., Enzmann, F., Kersten, M., 2015. From connected pathway flow to ganglion dynamics. Geophys. Res. Lett. 42, 3888–3894. https://doi.org/10.1002/2015GL064007

Sanna, A., Dri, M., Hall, M.R., Maroto-Valer, M., 2012. Waste materials for carbon capture and storage by mineralisation (CCSM) - A UK perspective. Appl. Energy 99, 545–554. https://doi.org/10.1016/j.apenergy.2012.06.049

Sarkar, G., Siddiqua, S., 2016. Effect of fluid chemistry on the microstructure of light backfill: An X-ray CT investigation. Eng. Geol. 202, 153–162. https://doi.org/10.1016/J.ENGGEO.2016.01.012

Schindelin, J., Arganda-Carreras, I., Frise, E., Kaynig, V., Longair, M., Pietzsch, T., Preibisch, S., Rueden, C., Saalfeld, S., Schmid, B., Tinevez, J.Y., White, D.J., Hartenstein, V., Eliceiri, K., Tomancak, P., Cardona, A., 2012. Fiji: An open-source platform for biological-image analysis. Nat. Methods 9, 676–682. https://doi.org/10.1038/nmeth.2019

Schlüter, S., Sheppard, A., Brown, K., Wildenschild, D., 2014. Image processing of multiphase images obtained via X-ray microtomography: A review. Water Resour. Res. 50, 3615–3639. https://doi.org/10.1002/2014WR015256

Schuiling, R.D., Krijgsman, P., 2006. Enhanced weathering: An effective and cheap

tool to sequester CO2. Clim. Change 74, 349–354. https://doi.org/10.1007/s10584-005-3485-y

Scott, P.W., Critchley, S.R., Wilkinson, F.C.F., 1986. The chemistry and mineralogy of some granulated and pelletized blastfurnace slags. Mineral. Mag. 50, 141–148.

Sengur, A., Budak, U., Akbulut, Y., Karabatak, M., Tanyildizi, E., 2019. A survey on neutrosophic medical image segmentation, in: Guo, Y., S. Ashour, A. (Eds.), Neutrosophic Set in Medical Image Analysis. Elsevier, pp. 145–165. https://doi.org/10.1016/B978-0-12-818148-5.00007-2

Shah, S.M., Gray, F., Crawshaw, J.P., Boek, E.S., 2016. Micro-computed tomography pore-scale study of flow in porous media: Effect of voxel resolution. Adv. Water Resour. 95, 276–287. https://doi.org/10.1016/j.advwatres.2015.07.012

Singh, A., Armstrong, R., Regenauer-Lieb, K., Mostaghimi, P., 2019. Investigating rock micro-structure of sandstones by pattern recognition on their X-ray images. ASEG Ext. Abstr. 2019, 1–3. https://doi.org/10.1080/22020586.2019.12073166

Ter Teo, P., Seman, A.A., Basu, P., Sharif, N.M., 2016. Characterization of EAF Steel Slag Waste: The Potential Green Resource for Ceramic Tile Production. Procedia Chem. 19, 842–846. https://doi.org/10.1016/j.proche.2016.03.111

Turner, C.H., Brennan, J.K., Pikunic, J., Gubbins, K.E., 2002. Simulation of chemical reaction equilibria and kinetics in heterogeneous carbon micropores. Appl. Surf. Sci. 196, 366–374. https://doi.org/10.1016/S0169-4332(02)00074-0

van Eijnatten, M., van Dijk, R., Dobbe, J., Streekstra, G., Koivisto, J., Wolff, J., 2018. CT image segmentation methods for bone used in medical additive manufacturing. Med. Eng. Phys. 51, 6–16.

https://doi.org/10.1016/J.MEDENGPHY.2017.10.008

Vincent, L., Soille, P., 1991. Watersheds in Digital Spaces: An Efficient Algorithm Based on Immersion Simulations. IEEE Trans. Pattern Anal. Mach. Intell. 13, 583–598. https://doi.org/10.1109/34.87344

Wildenschild, D., Sheppard, A.P., 2013. X-ray imaging and analysis techniques for quantifying pore-scale structure and processes in subsurface porous medium systems. Adv. Water Resour. 51, 217–246. https://doi.org/10.1016/j.advwatres.2012.07.018

Wilson, S.A., Dipple, G.M., Power, I.M., Thom, J.M., Anderson, R.G., Raudsepp, M., Gabites, J.E., Southam, G., 2009. Carbon dioxide fixation within mine wastes of ultramafic-hosted ore deposits: Examples from the Clinton Creek and Cassiar Chrysotile deposits, Canada. Econ. Geol. 104, 95–112. https://doi.org/10.2113/gsecongeo.104.1.95

Yadav, S., Mehra, A., 2017. Experimental study of dissolution of minerals and CO2 sequestration in steel slag. Waste Manag. 64, 348–357. https://doi.org/10.1016/j.wasman.2017.03.032

You, K., Lee, S.-H., Hwang, S.-H., Kim, H., Ahn, J.-W., 2011. CO₂ Sequestration via a Surface-Modified Ground Granulated Blast Furnace Slag Using NaOH Solution. Mater. Trans. 52, 1972–1976. https://doi.org/10.2320/matertrans.M2011110

Zachara, J., Brantley, S., Chorover, J., Ewing, R., Kerisit, S., Liu, C., Perfect, E., Rother, G., Stack, A.G., 2016. Internal Domains of Natural Porous Media Revealed: Critical Locations for Transport, Storage, and Chemical Reaction. Environ. Sci. Technol. 50, 2811–2829. https://doi.org/10.1021/acs.est.5b05015

Zevenhoven, R., Kavaliauskaite, I., 2004. Mineral carbonation for long-term CO2

storage: An exergy analysis. Int. J. Thermodyn. 7, 23–31.

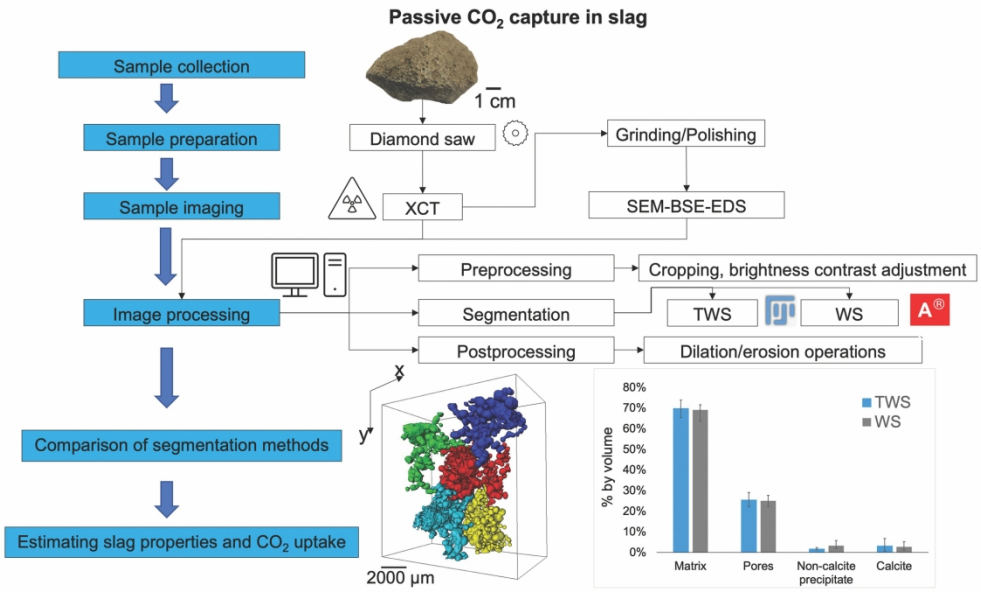

Graphical Abstract

189x113mm (300 x 300 DPI)

Table 1. Parameters of analysis techniques used in this study

XCT settings	
Source to object distance (mm)	35.0
Voltage (kV)	90
Current (μA)	111
Exposure time (s)	1.415
Number of projections taken	3141
Voxel size (x=y=z, μm)	10.368
SEM settings	
Accelerating voltage (kV)	20
Aperture (μm)	60
Working Distance (mm)	8.5
Pixel size (μm)	2.407

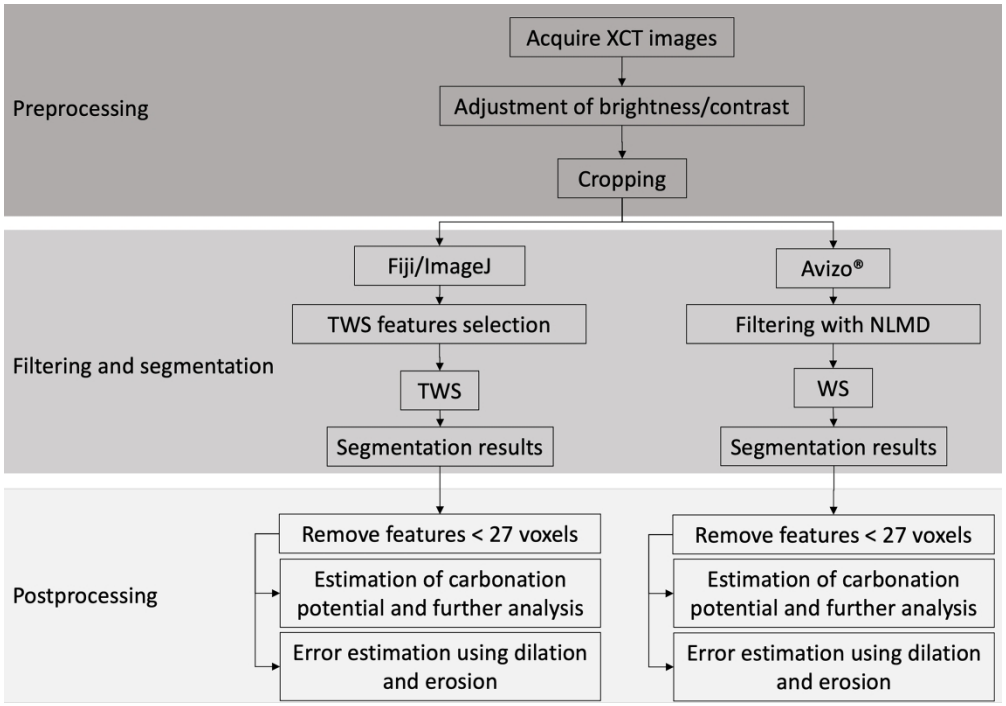

Fig. 1. A schematic flowchart summarizing the steps of the different image processing pipelines used in this study.

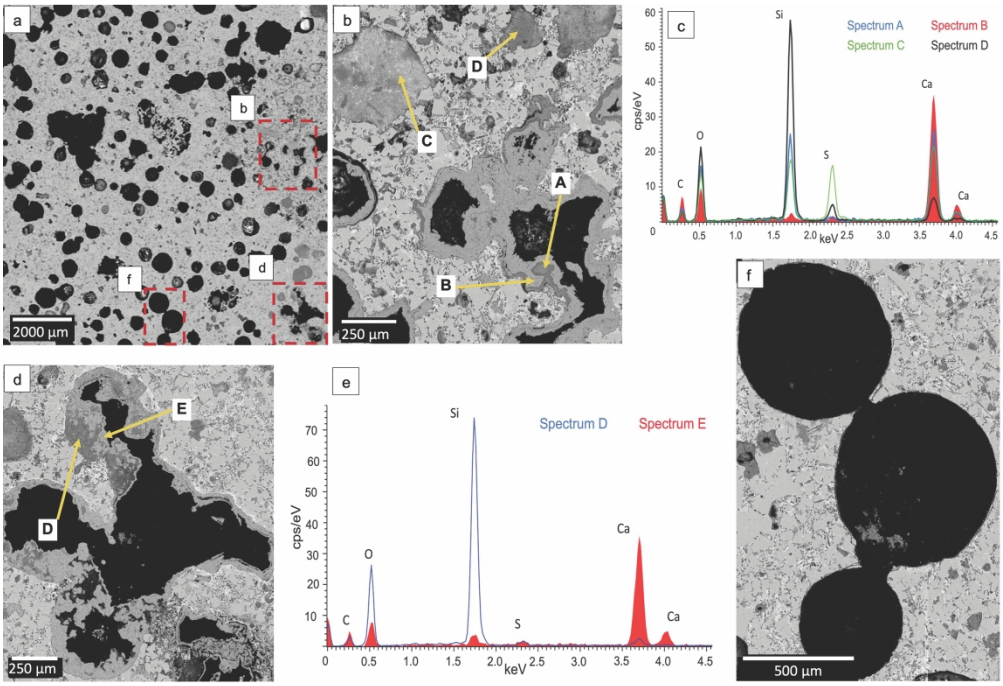

Fig. 3. SEM imaging results. (a) BSE image of the studied sample, also defining magnified regions shown in (b), (d) and (f). (c) and (e) are spectra that show the compositions noted in figures (b) and (d), respectively. (f) portrays the texture and microporosity of the studied sample.

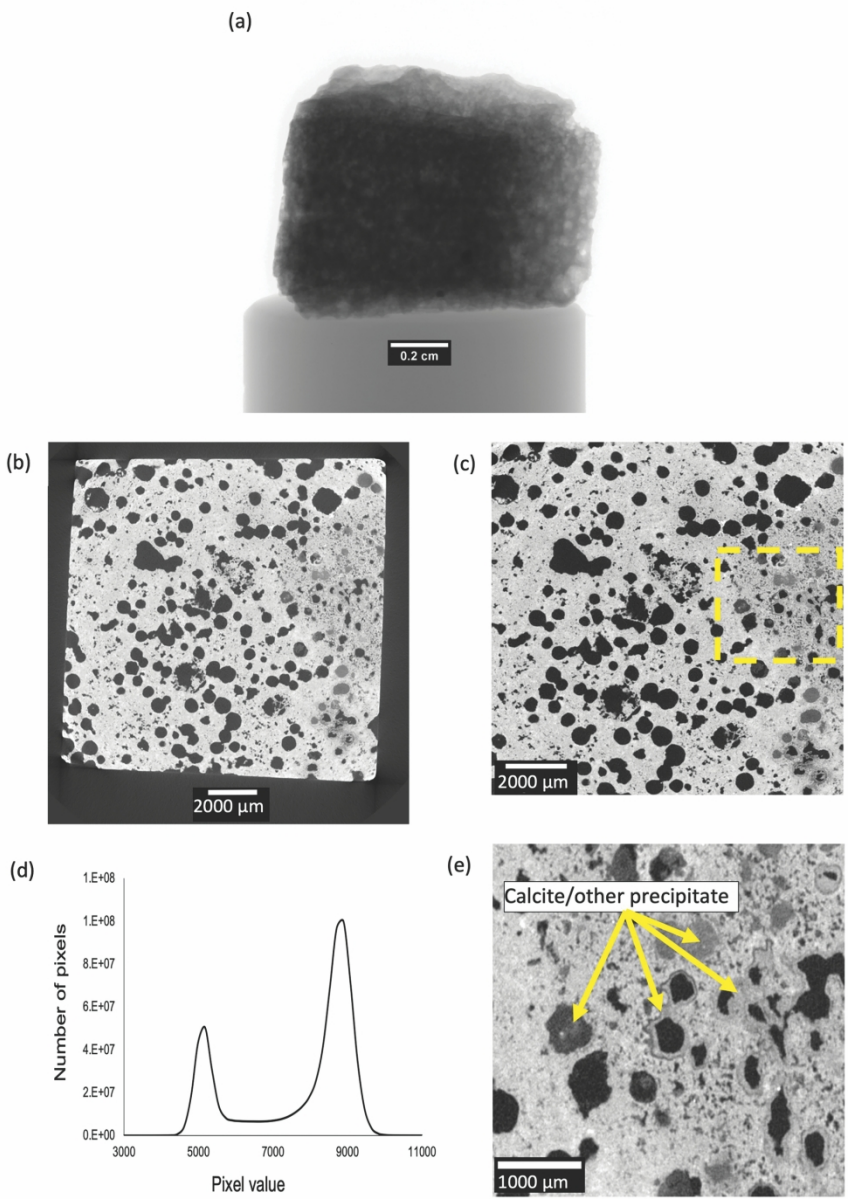

Fig. 2. Results obtained from XCT analysis. (a) X-ray projection; (b) reconstructed cross-sectional image; (c) image shown in (b) after cropping and adjustment of brightness/contrast; (d) histogram of the collected XCT images; (e) magnification of boxed area in (c).

160x225mm (300 x 300 DPI)

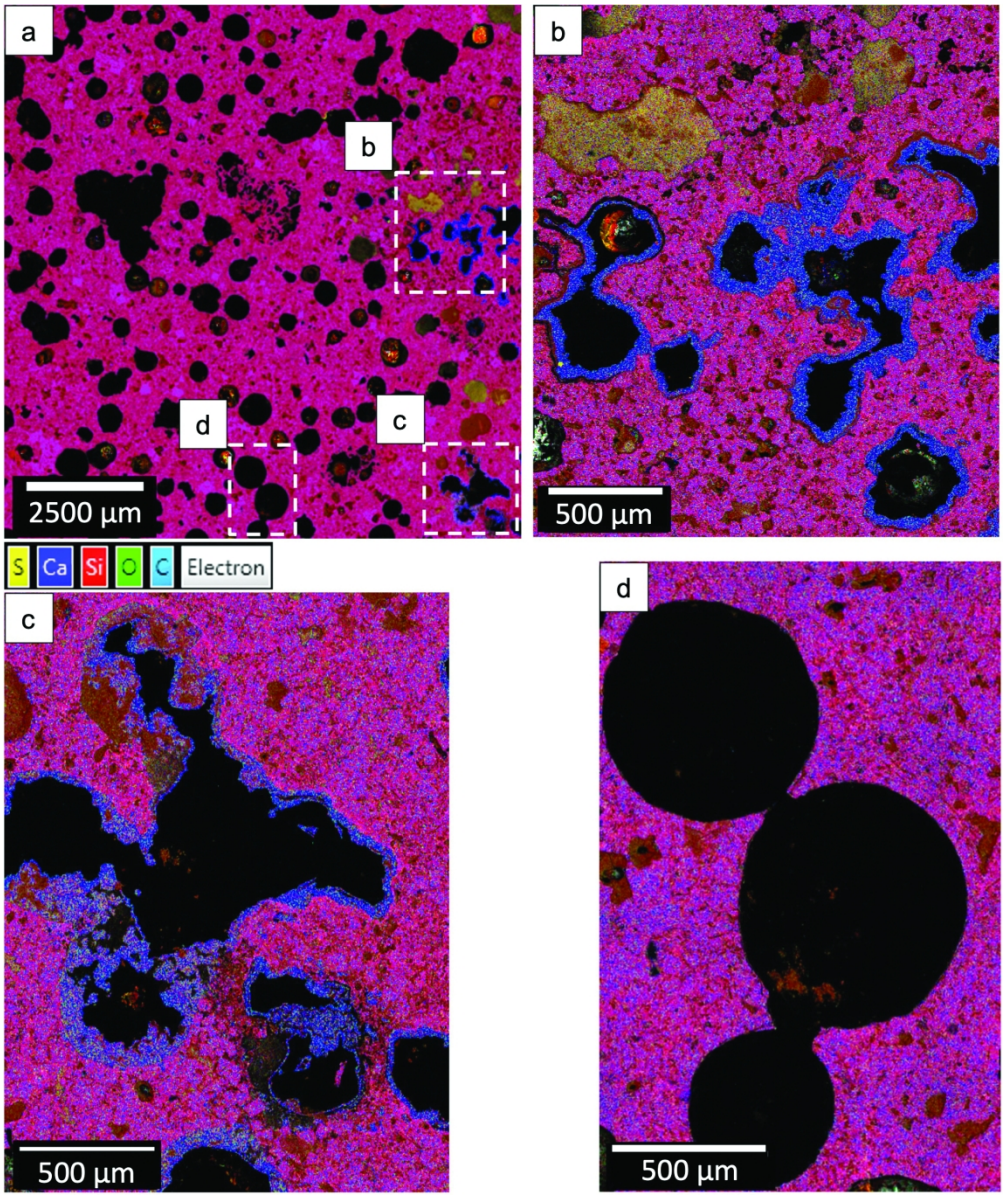

Fig. 4. False colour SEM-EDS elemental maps for different elements present in the studied slag sample. Boxed areas in (a) define magnified areas in (b), (c), and (d).

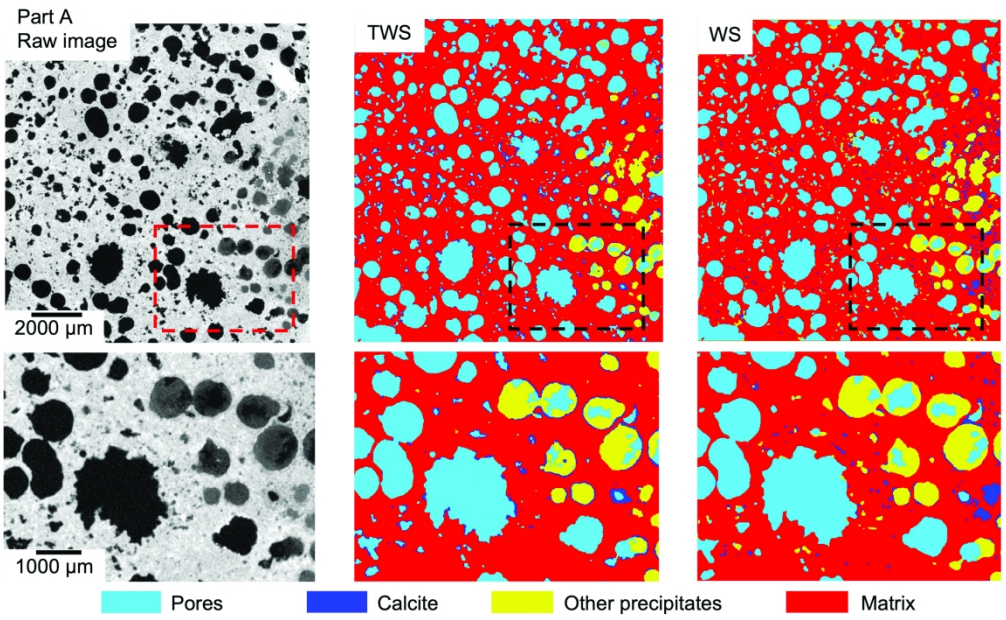

Fig. 5. Segmentation results. Bottom row is a zoomed in image of the area defined by the box in the top right. Boxed areas in images a, b and c are zoomed in the images in the bottom row. This figure is continued on the next page.

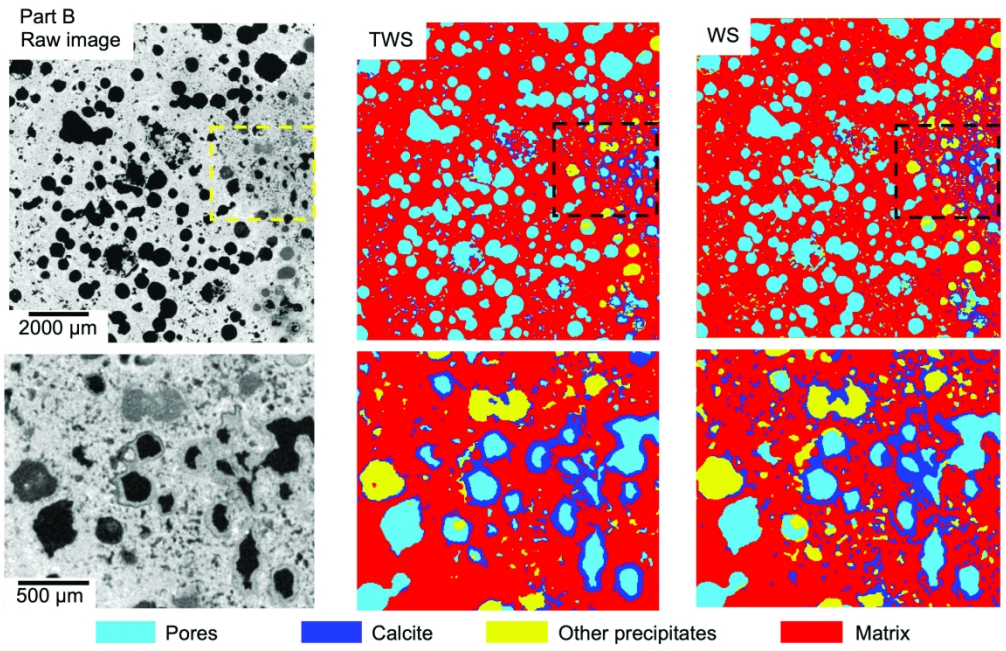

Fig. 5 continued

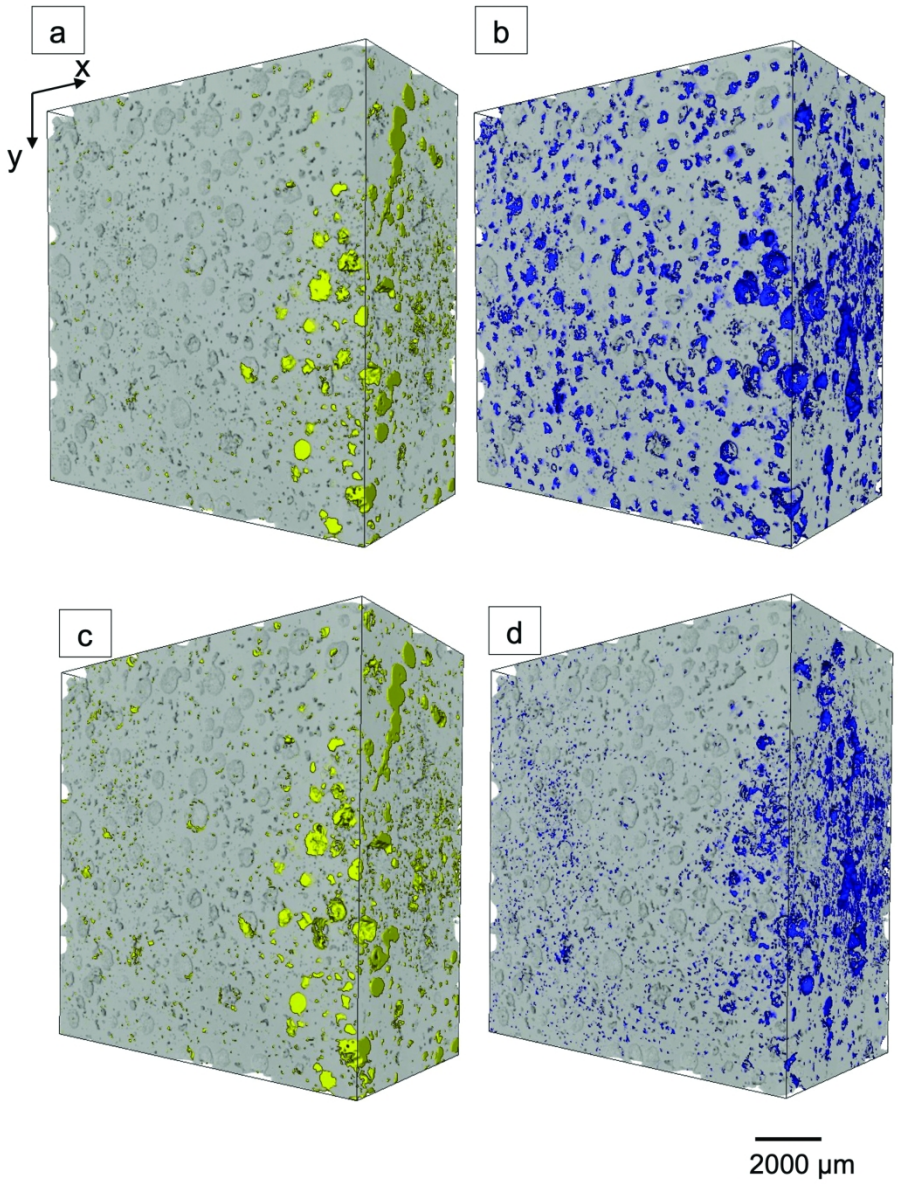

Fig. 6. Segmentation results of precipitate and calcite. (a) and (b) are non-calcite precipitate and calcite distribution, respectively, as obtained from TWS. (c) and (d) are non-calcite precipitate and calcite, respectively, as obtained from WS.

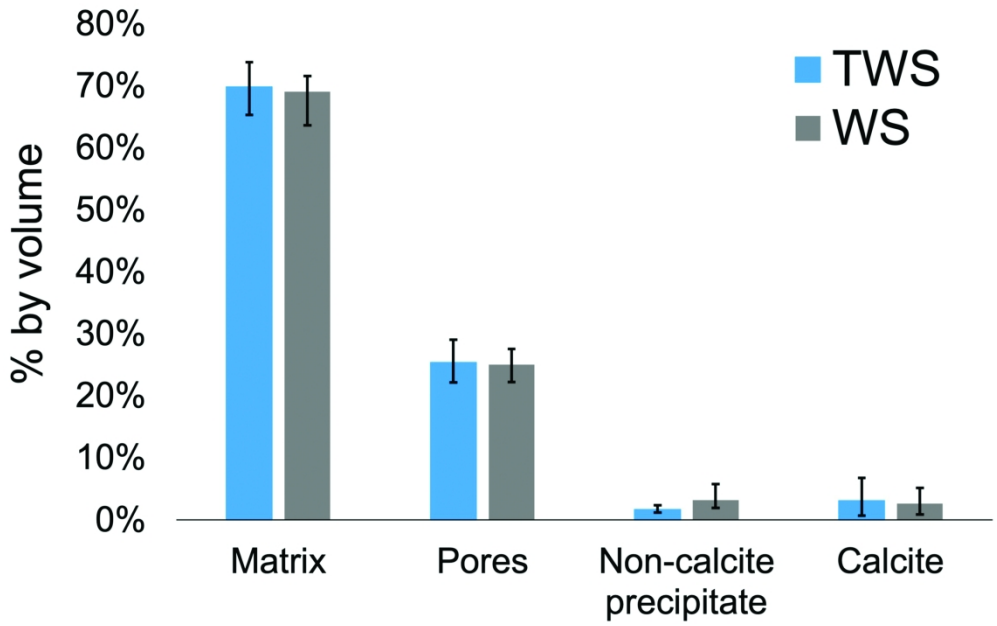

Fig. 7. Volume fraction of different phases as calculated from TWS and WS. Error bars are produced by a plying dilation and erosion operations to segmentation results.

Table 2. Some transport properties of slag obtained from two different segmentation techniques

Property	TWS	Watershed
Total porosity (%)	25.4	25.1
Surface area (μm^2)	3.38×10^9	2.91×10^9
Mean equivalent diameter (μm)	120	162

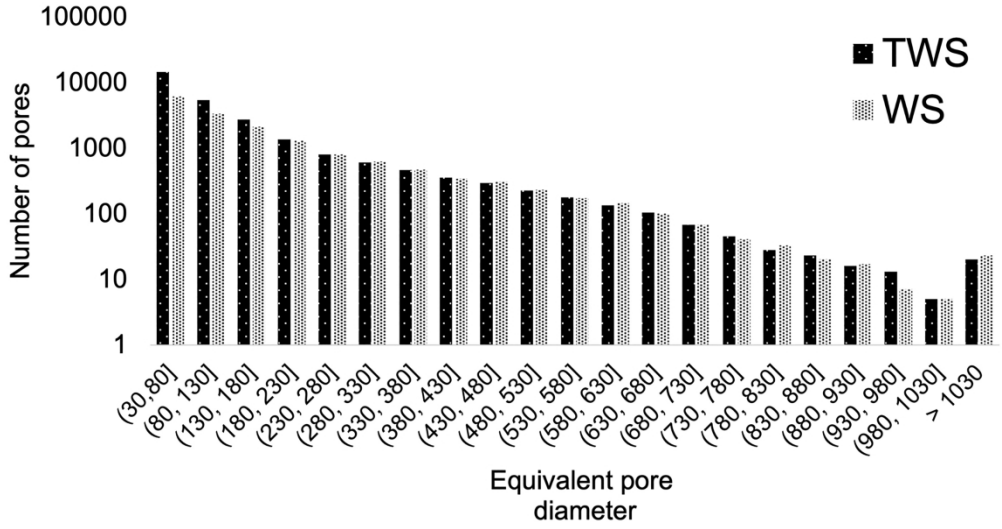

Fig. 8. Pore equivalent diameters distribution in the slag sample as calculated from TWS and WS, respectively.

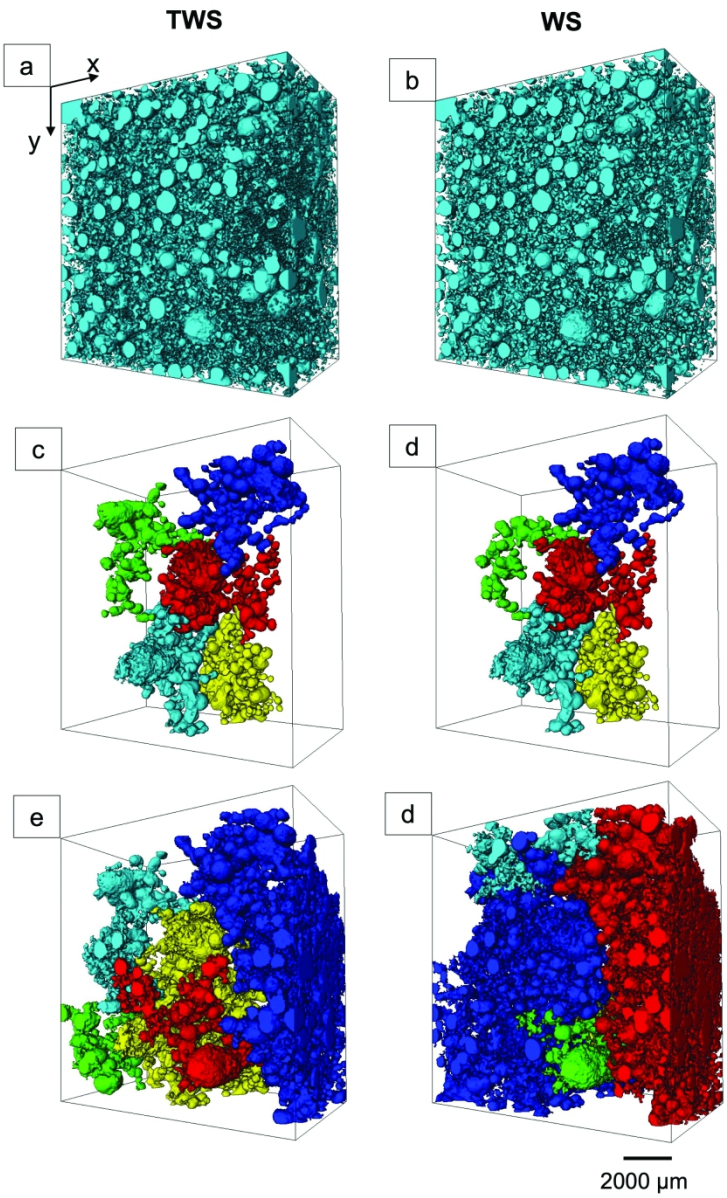

Fig. 9. Analysis of pore space as segmented by TWS (left column) and WS (right column). Images (a) and (b) depict the total porosity of the sample. Images (b) and (c) reveal the largest five connected pore spaces, each with a distinct color. Images (e) and (f) reveal the largest five connected pore spaces prior to precipitation.

Supplementary Information for

Image-based analysis of weathered slag for calculation of transport properties and passive carbon capture

Faisal W. K. Khudhur [1]*, Alice Macente[1, 2], John M. MacDonald [1], Luke Daly [1,3,4]

[1] School of Geographical and Earth Science, University of Glasgow, Glasgow G12 8QQ, UK

[2] Department of Civil and Environmental Engineering, University of Strathclyde, Glasgow, G1 1XJ

[3] Centre for Microscopy and Microanalysis, University of Sydney, Sydney, 2006 NSW, Australia

[4] Department of Materials, University of Oxford, Oxford, OX1 3PH, UK

*Corresponding author: f.khudhur.1@research.gla.ac.uk

Content description:

S1. Alignment steps of the BSE 2D image with a slice within the XCT 3D volume

The following steps describe the procedure followed to align the high-resolution backscattered image (BSE) that has a resolution of 2.407 µm with the corresponding XCT slice within the studied volume that has a resolution of 11.72 µm. This procedure is summarized in Fig. S1.

1. First, a sub-volume that surrounds the area in which the dissection of the sample occurred was identified, as depicted in Fig. S1 (a).
2. A slice module was used to search for the slice that matches the BSE image. This slice was extracted for numerical comparison with the BSE image (see point 4).
3. The BSE image was aligned with the XCT slice by rotating the former until it matches the latter. The *align module* in Avizo ® 9.3.0 was used for this purpose (after resampling of the BSE image).
4. The coefficient of correlation metric was calculated using the *corr2* syntax in Matlab (Mathworks, 2022).

The slice that was obtained using this method is well-aligned with the BSE image, with a correlation coefficient value of 0.7. Values between 0.6-0.8 are common when registering BSE and XCT images (Latham et al., 2008).

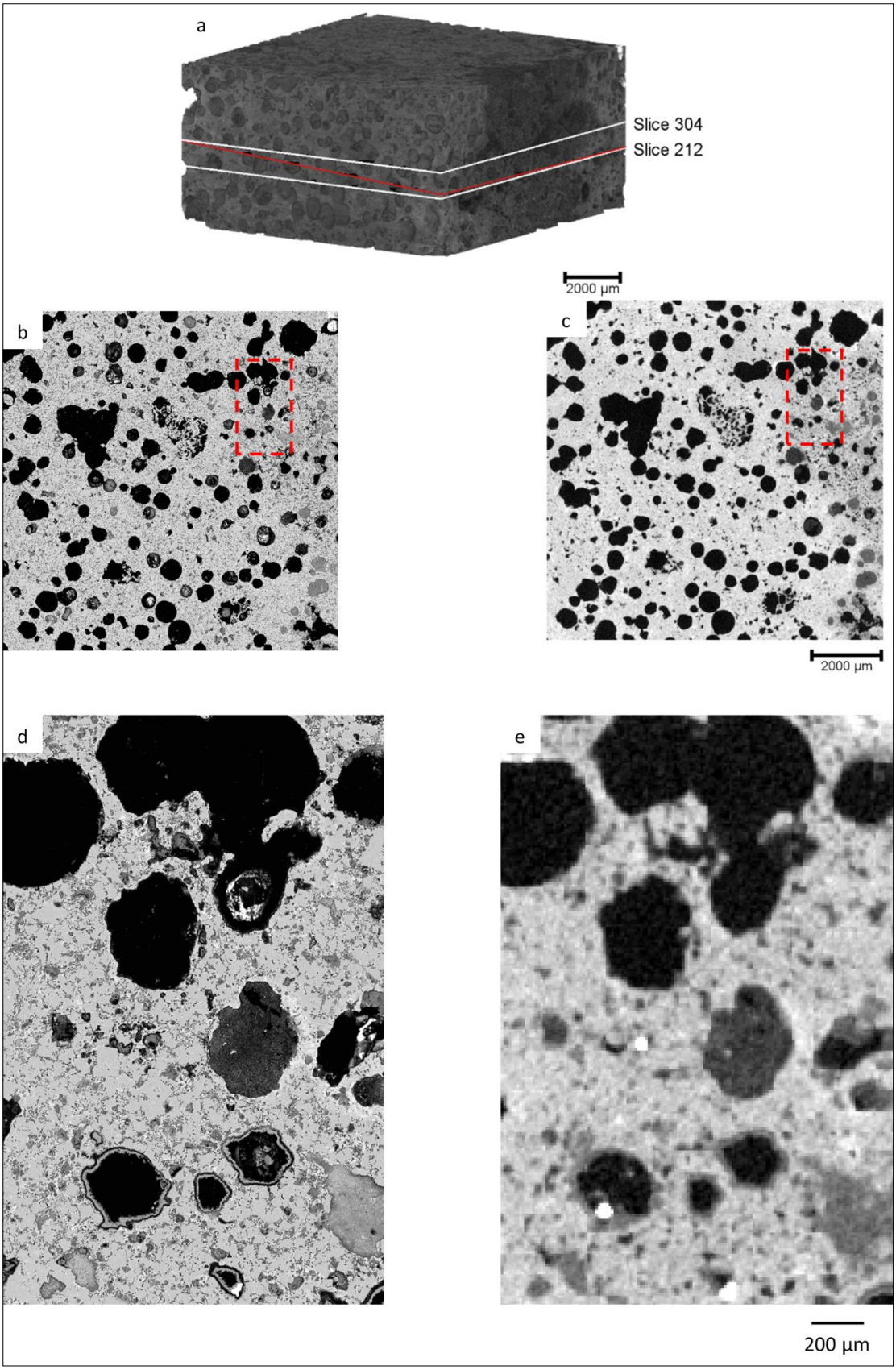

Fig. S1. Registration of high-resolution BSE image with the corresponding slice in the 3D volume. (a) The studied volume, showing the slice of interest in red; (b) high resolution BSE image; (c) the corresponding slice in the studied volume; (d) and (e) are the boxed areas in (b) and (c), respectively.

S2. Remarks about the TWS

The TWS plugin in Fiji provides a graphical user interphase (GUI) that enables users to perform machine learning-based segmentation. For each class, several pixels are identified and annotated by the user, and they are used to generate several decision trees through the bootstrap aggregation (Bulgarevich et al., 2018). In bootstrap aggregation, the data that form the decision trees are randomly selected from the training set, with replacement, and decision trees can be generated based on different measures such as the Gini index, information gain and variance. Decision trees are generated based on several features that the user defines. In image processing, these features can be noise reduction features, such as the gaussian blur filter, edge detectors such as the Sobel filter and texture information such as the structure tensor. In this study, we used the default TWS classifier which is the fast random forest that uses 200 trees, constructed while considering 2 random features. This classifier uses feature randomness to make a forest of uncorrelated trees, and based on probability aggregation, the class of a particular pixel is identified as one of the prespecified classes (Bulgarevich et al., 2018; Purswani et al., 2020). The data that were not used in establishing the trees were used to evaluate the prediction of the classifier, by producing a metric known as the out-of-bag error. It reflects the percentage of pre-specified pixels that are wrongly segmented by the random forest classifier (Bulgarevich et al., 2018). The training algorithm with the lowest out-of-bag error is the one more suited for the classification. Fig S2 describes the workflow of the TWS in Fiji.

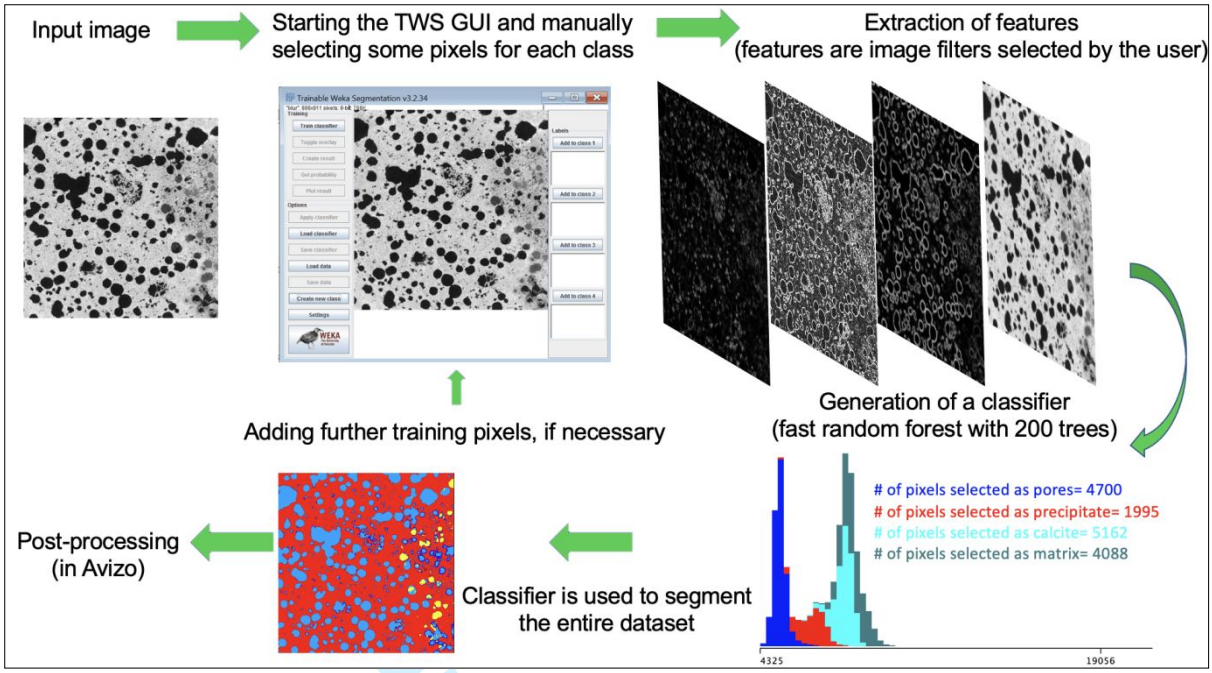

Fig. S2. Demonstration of TWS GUI.

Table S1. WEKA features selected for different training files.

File	Features							Number of features
1	GB*	DoG**	Membrane	Sobel		Hessian		76
2	GB		Membrane	Sobel		Hessian		66
3	GB			Sobel		Hessian		60
4	GB			Sobel				12
5	GB			Sobel	Laplacian			17
6	GB			Sobel	Laplacian		Entropy	37
7	GB			Sobel	Laplacian		Structure	37
8	GB			Sobel	Laplacian		Derivative	37
9	GB			Sobel	Laplacian		Neighbourhood	57
10	GB	DoG	Membrane	Sobel	Laplacian	Hessian	Derivative Neighbourhood	141
11	GB	DoG	Membrane	Sobel		Hessian		49
12	GB			Sobel			Derivative	32
13	GB			Sobel			Structure	32
14	GB			Sobel			Neighbourhood	52

GB: Gaussian blur. DoG: difference of gaussians. Default values for $\sigma_{min\ and}$ σ_{max} (i.e., minimum and maximum isotropic filter radii used in feature creation, respectively) were used except for set 11 where σ_{max} was reduced to 4.0

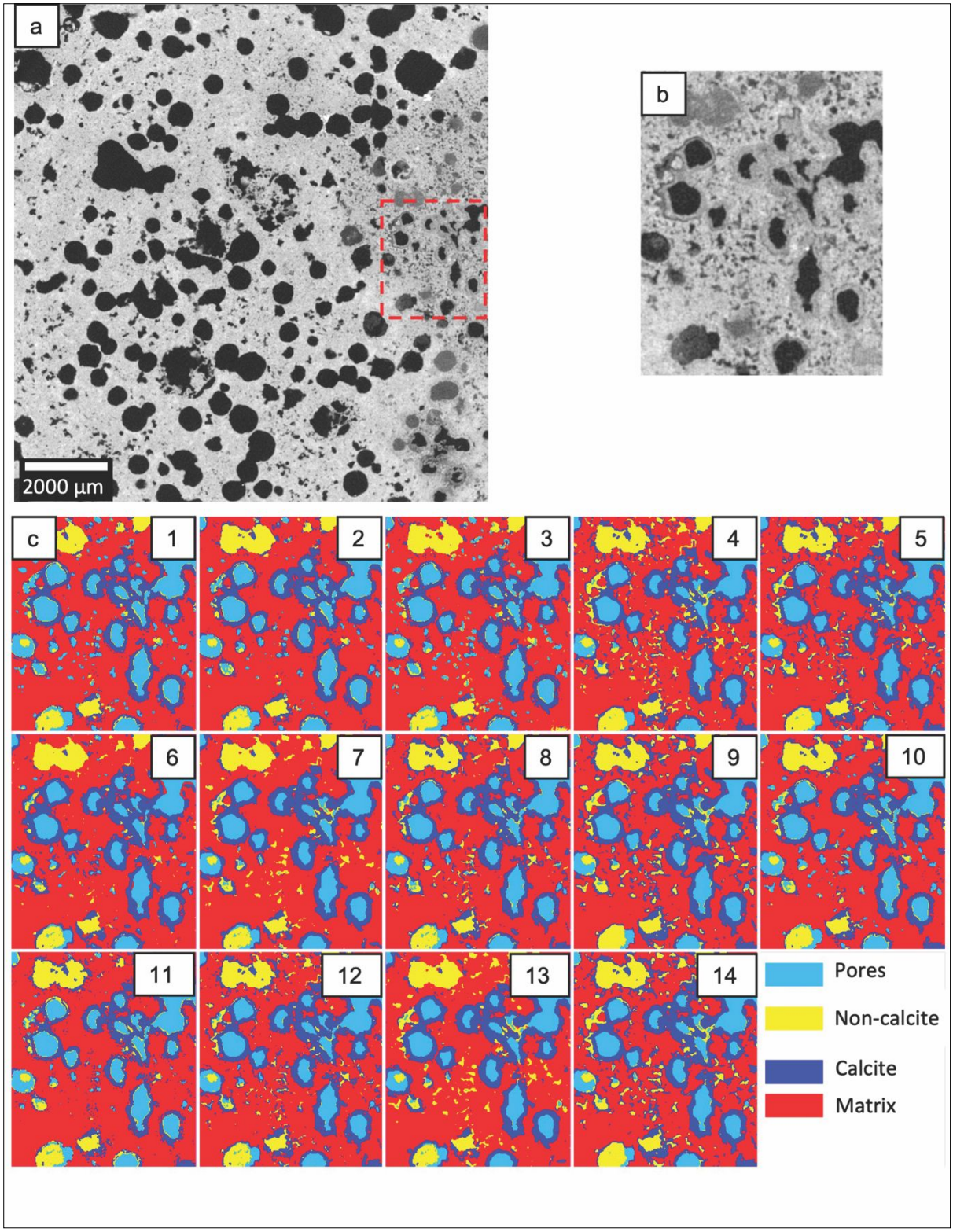

Fig. S3. Results of TWS using different training features. (a) a raw slice obtained from the XCT imaging; (b) magnification of the boxed area in (a); (c) TWS segmentation results as calculated by different training files.

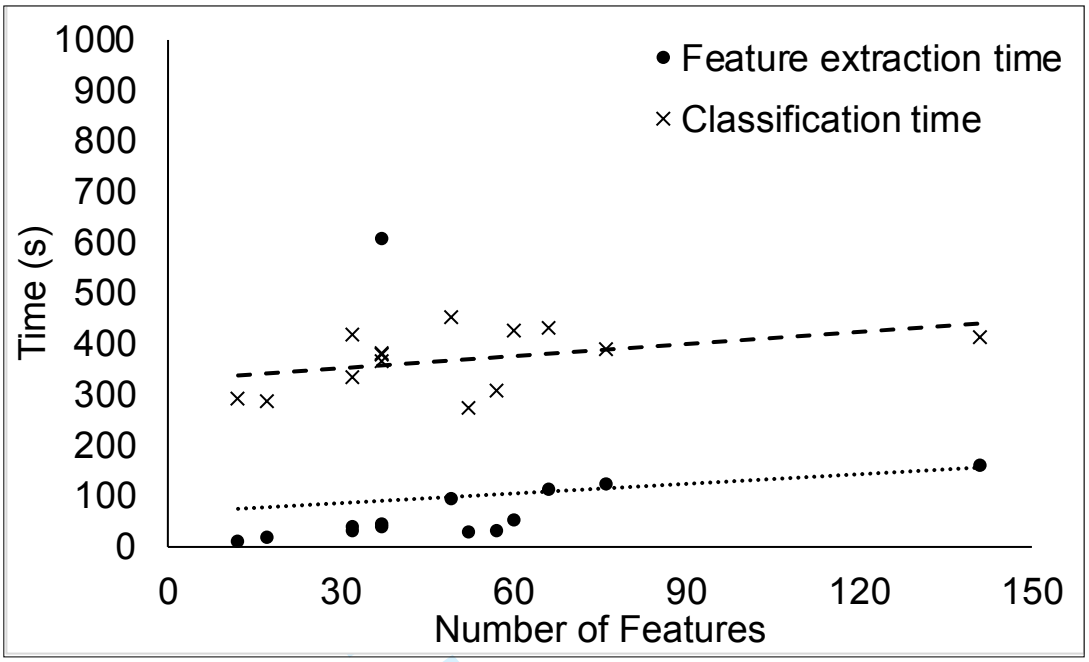

Fig. S4. Effect of the number of training features on the segmentation time. Straight lines represent the best fit lines for the different time categories

.

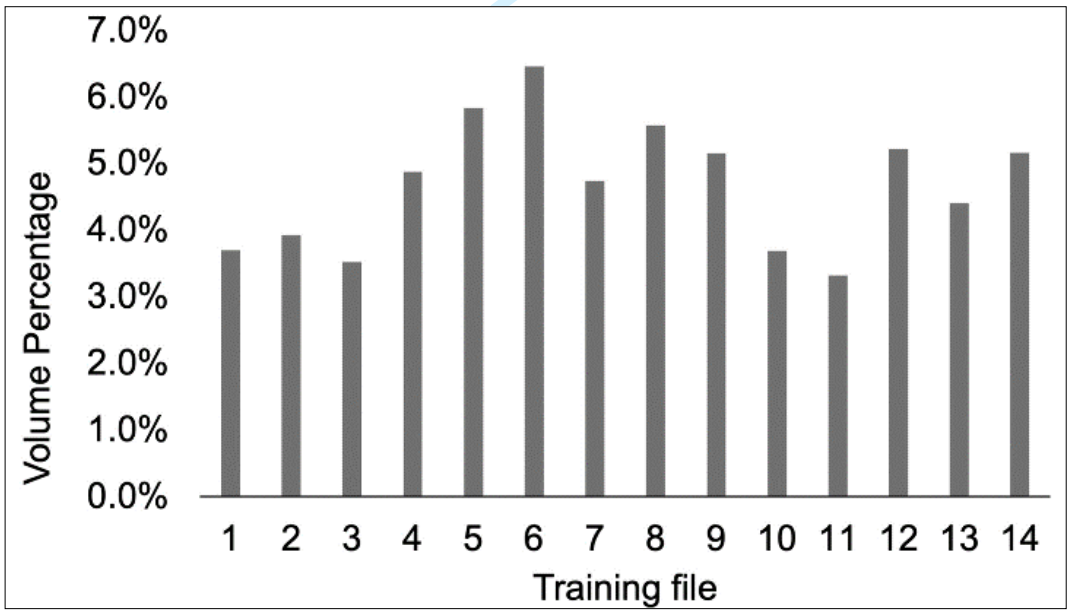

Fig. S5. The volume fractions of calcite predicted from the different training set.

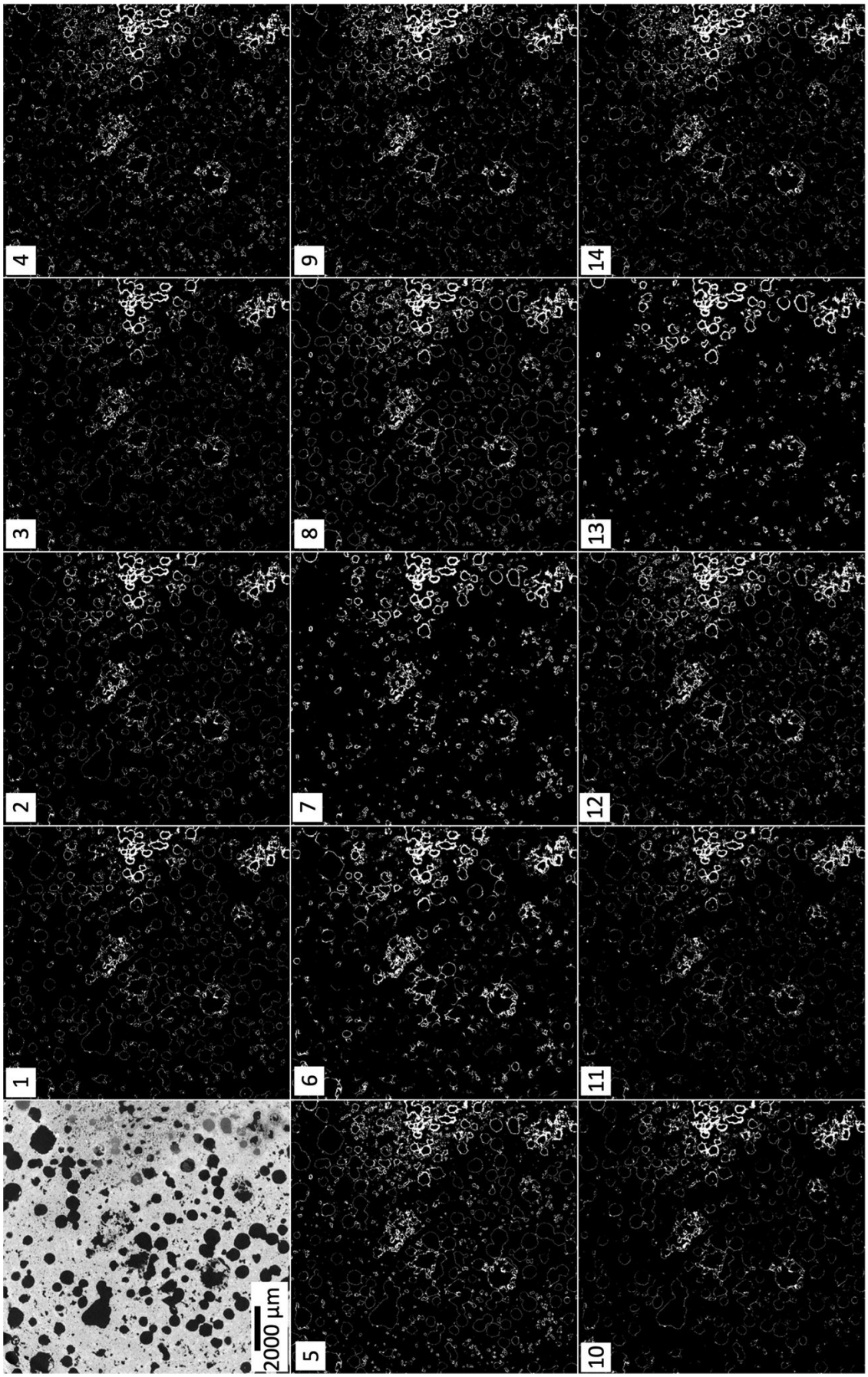

Fig. S6. Calcite distribution as predicted by TWS with different training files.

The results in Fig. S3 through Fig. S6 were used to identify the best training set according to the following criteria:

- Visual inspection of the 14 images of figures S3 and S6.
- Measuring the prediction quality of the machine learning classifier through comparison of out-of-bag error that TWS calculates for each segmentation file. The classifiers with the lowest out-of-bag error are the most suited for the classification.
- The complexity of the segmentation, which is reflected by the number of features. Ideally, a lower number of features makes the classification faster and easier.
- The time of segmentation.

We plotted these factors on a net diagram as shown in Fig. S7. Based on Fig. S7, we found that the training set 13 provides the best compromise between the number of features (13), out-of-bag error (0.276%) and processing time (6 mins). We therefore used it in segmenting the entire data set. Note that training sets 7 and 13 have less misclassification around the boundaries. Both sets contain the structure filter. This filter calculates the largest and smallest eigenvalues of the structure tensor for each element in the picture (Arganda-Carreras et al., 2017). This filter has been found to be more powerful in describing local patterns based on using local neighborhoods for data integration, and it has been used in enhancing image features and in textural analysis (Arseneau, 2006; Weickert, 1999). The segmentation of the entire dataset took around 2 hours. 30 minutes were required to annotate training pixels, while 90 minutes were needed for the segmentation process to be finished. If results were not satisfactory, additional pixels were added iteratively until satisfactory results were obtained. **In the current study, this operation is executed for 5. This amount of repetitions was sufficient to observe that adding further training pixels does not result in further improvement.**

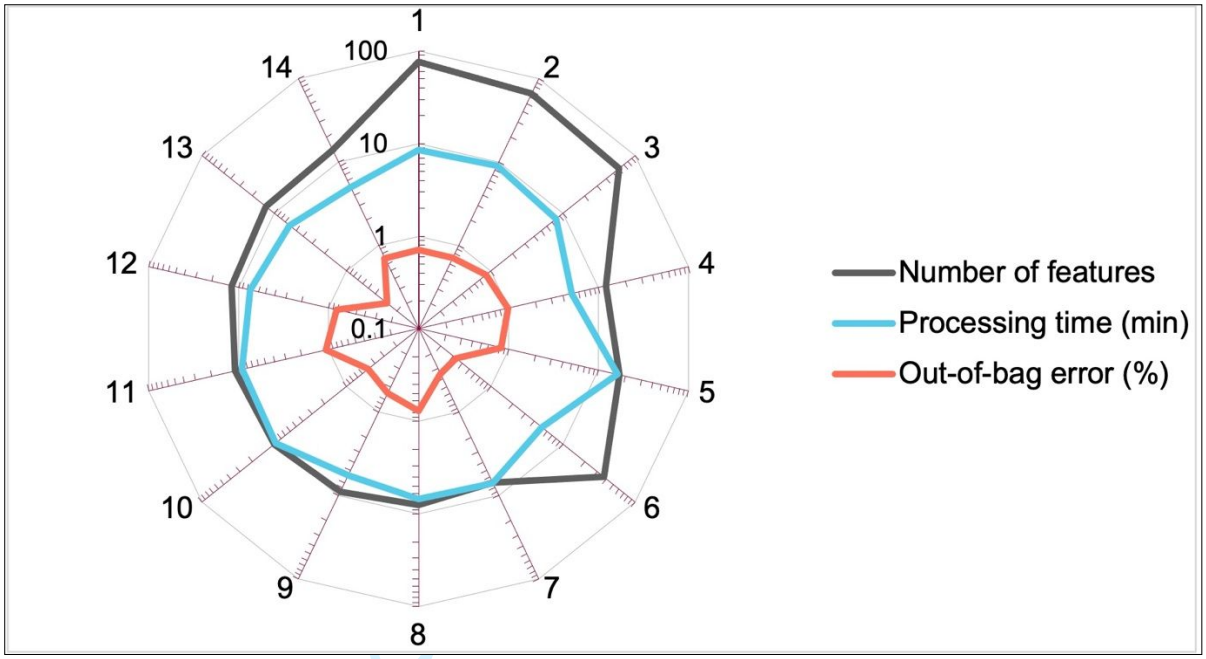

Fig. S7. Representation of the number of features, processing time and out-of-bag error of the different training files that are presented in Table S1. The values on the circumference of the circle (from 1 to 14) represent the training files that are shown in Table S1. The logarithmic axes that are on the radii of the circle are used to find the values of the number of features, processing time and out-of-bag error, in the units shown in the legend of the figure.

S3. Filtering and Watershed Segmentation

The watershed segmentation wizard in Avizo ® 9.3.0 was used to segment the dataset into pores, precipitates, calcite and matrix. Watershed segmentation strongly depends on noise, making filtering essential (Preim and Botha, 2014). Prior to the segmentation, non-local means denoising (NLMD) was used, with a search window of 20 pixels, a local neighborhood of 5 pixels, and a similarity value of 0.4. The effect of NLMD on noise reduction is illustrated in Fig. S8. For the watershed segmentation wizard, the following parameters were used:

- Gradient threshold = 1250
- Threshold for pores = 0 - 5620
- Threshold for precipitates = 5700 - 6850
- Threshold for calcite = 7550 - 8020
- Threshold for matrix= 8050 – 50384

These ranges are depicted on Fig S8 (c). The watershed segmentation did not take any considerable time (~10 min), though some time was needed to find the best parameters (~ 1 hour).

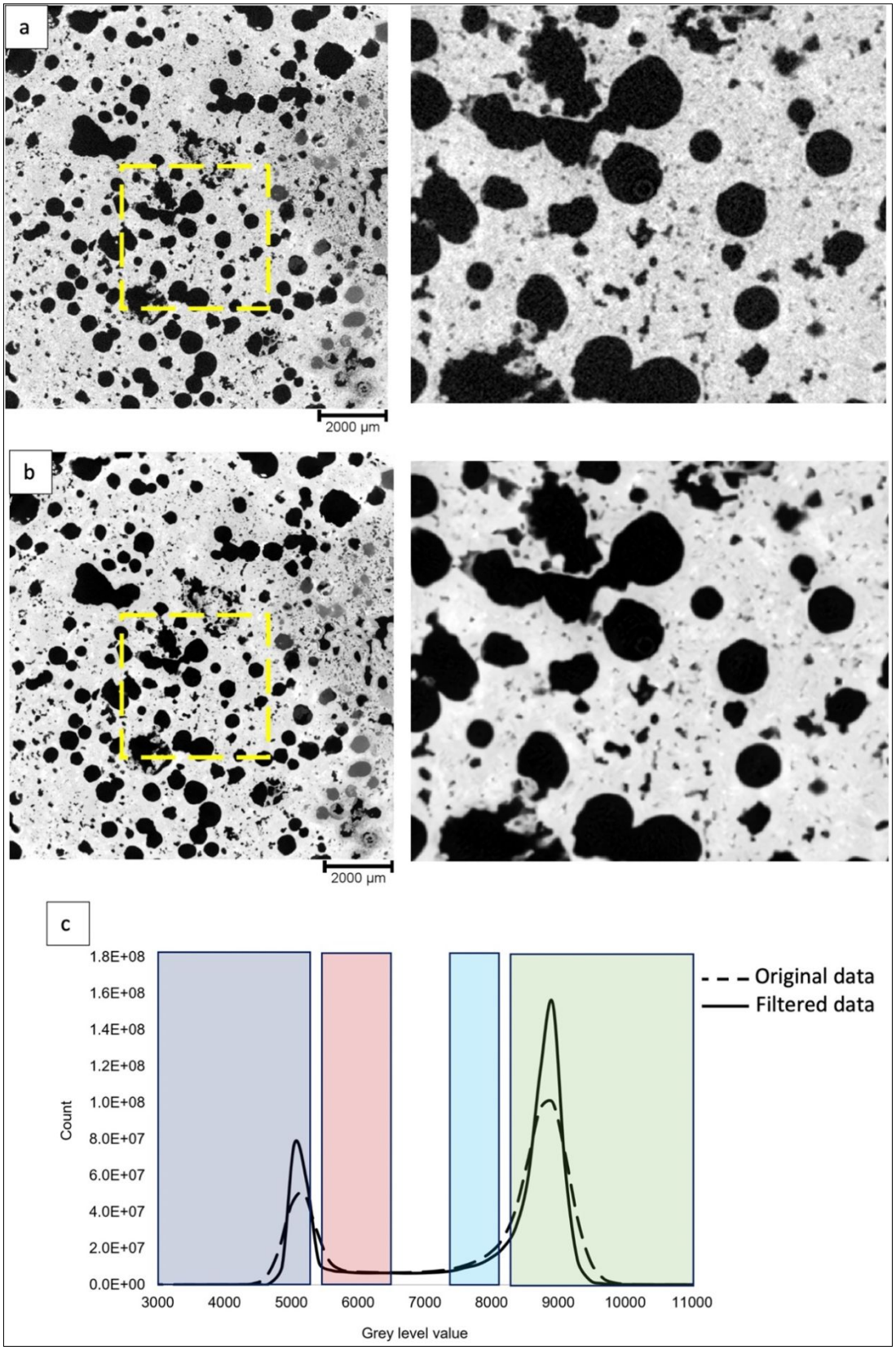

Fig. S8. Effect of NLMD on image segmentation. (a) a raw image and a close-up image as highlighted by the yellow dashed line (b) the corresponding filtered image and a close-up image. (c) the histogram of raw and filtered images, with the dashed line representing the raw dataset and the solid line representing the filtered dataset. The boxes on the histogram, from left to right, represent the threshold range that was specified in the watershed segmentation for the pores (blue), the precipitate (pink), calcite (light blue) and matrix (light green) respectively.

S4. Further comparison between TWS and WS

The high-resolution BSE image was also segmented using TWS and WS, and the area fractions of the different classes were compared with the corresponding slice that was obtained using XCT and segmented using both pipelines. The results are depicted in Fig. S9. Segmentation of the high-resolution BSE image reveals a higher fraction of precipitate when compared to the corresponding value obtained from the segmentation of the lower resolution XCT image. This is attributed to precipitation in smaller pores that were not detected in the XCT imaging due to the resolution limitation.

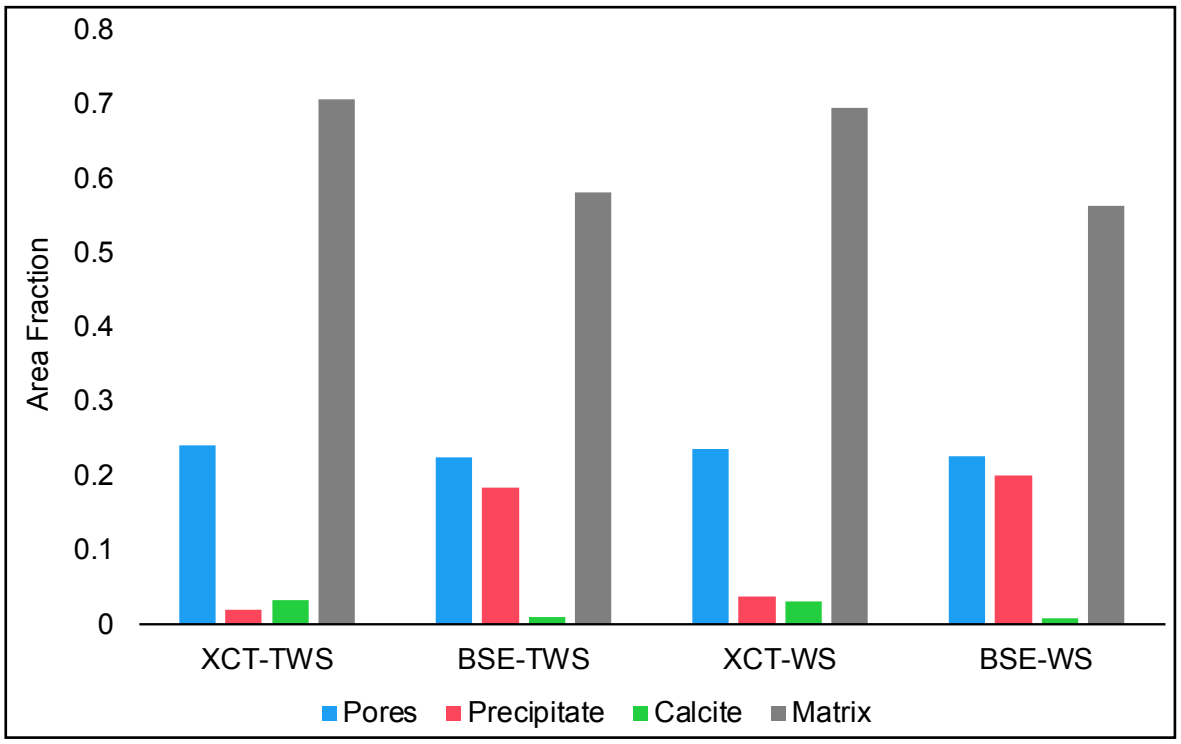

Fig. S9. Comparison of area fraction based on segmentation of XCT slice with TWS (XCT-TWS), BSE slice with TWS (BSE-TWS), XCT slice with WS (XCT-WS) and BSE slice with WS (BSE-WS)

S5. Conventional analysis results

The TGA analysis has been widely used to estimate the amount of calcium carbonate in carbonated slag (Crouzet et al., 2017). The TGA result is reported as weight loss as a function of temperature. As the temperature range for calcite decomposition overlaps with the temperature decomposition ranges of other minerals, TGA analysis overestimates the calcite content. Consequently, modified graphical methods can be used to reduce this overestimation (Pan et al., 2016). This method is based on the extrapolation of the TGA curve to find the initial and final calcite decomposition temperature and recording the associated weight loss. This weight loss represents the fraction of CO_2 in the studied sample. For the studied slag, the weight loss as a function of temperature is depicted in Fig. S10, indicating a weight loss of 2.84% due to $CaCO_3$ decomposition. This is equivalent to 29 kg CO_2 / 1000 kg slag.

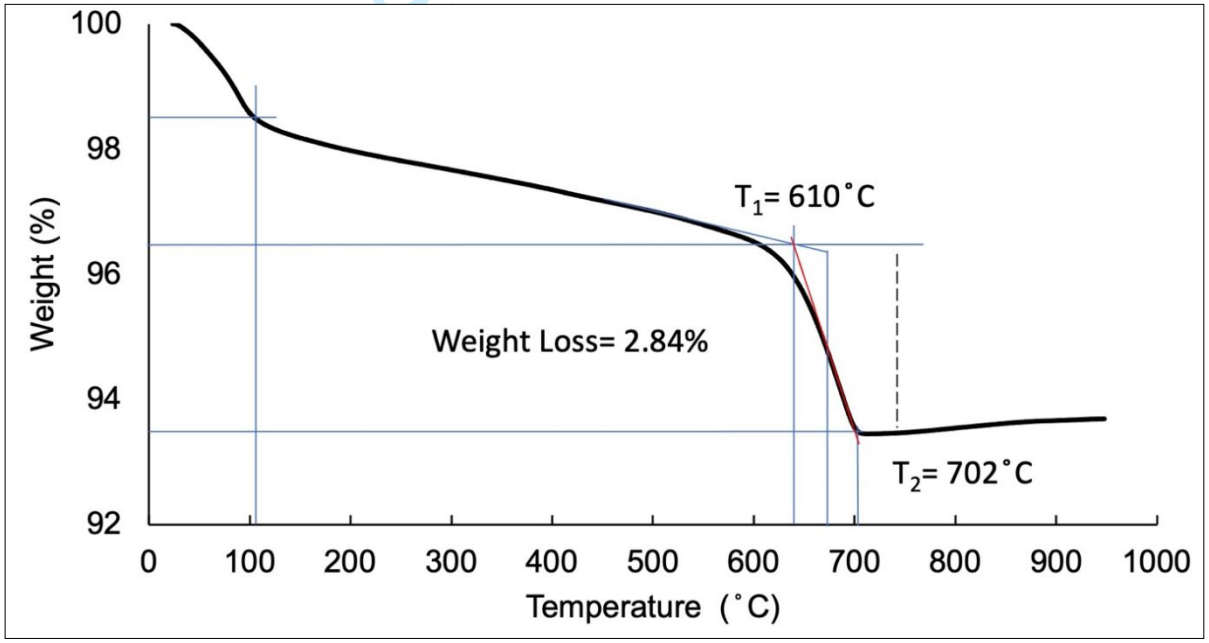

Fig. S10. Result of the thermogravimetric analysis. The weight loss due to calcite decomposition was found to be 2.84%, calculated based on the modified method reported in Pan et al. (2016) to reduce overestimation T_1 and T_2 represent the initial and final temperatures for $CaCO_3$ decomposition, respectively.

To have a better understanding of minerals presence in the studied slag, XRD analysis was utilized, and the diffraction patterns are shown in Fig. S11.

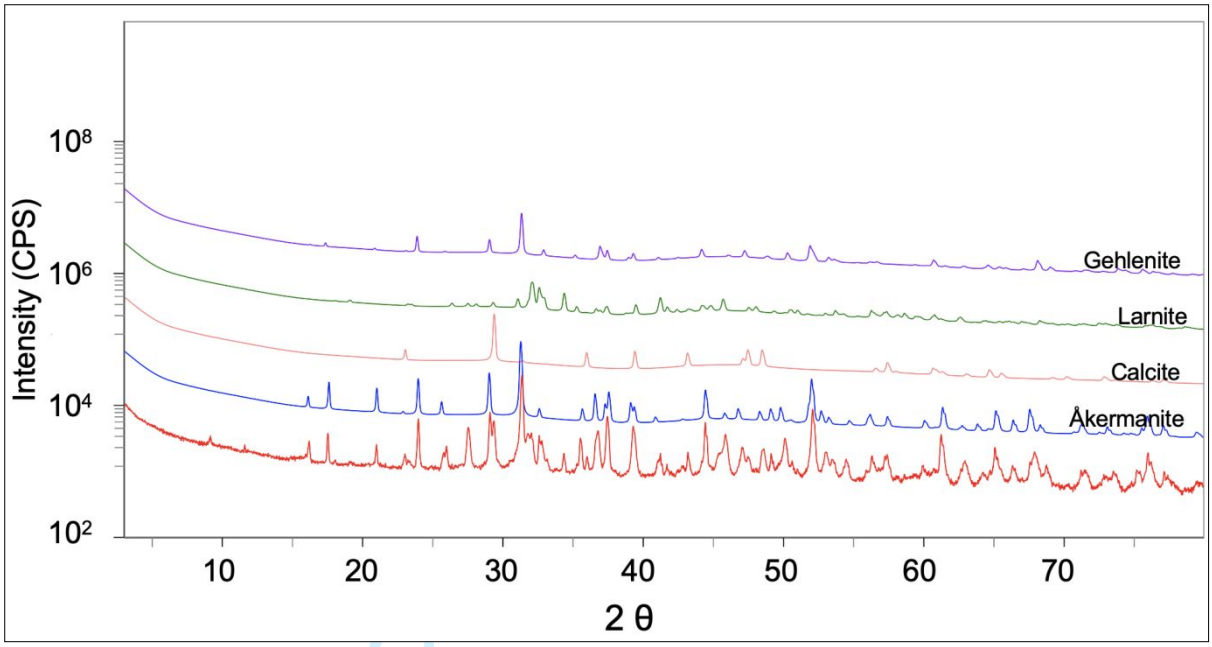

Fig. S11. Results of the XRD analysis, demonstrating the presence of calcite and the diffraction patterns of several common slag-forming minerals. The bottom line represents the diffraction pattern of the analyzed sample.

S6. EDS Spectra collected from different points within the studied sample

To understand the distribution of elements d within the studied sample, several spectra were collected from various points, as depicted in Fig. S12. Spectra A and B were collected near the area where most of the observed calcite precipitated, while spectra C, D and E were collected from locations where no significant calcite was observed. As the elements distribution and spectra are similar, it is difficult to identify the mineral distribution of slag, particularly as several slag minerals contain identical elements, such as åkermanite ($Ca_2MgSi_2O_7$) and merwinite ($Ca_3Mg(SiO_4)_{2)}$, or different polymorphs such β-Ca_2SiO_4 and γ-Ca_2SiO_4 (Chukwuma et al., 2021; Kriskova et al., 2013).

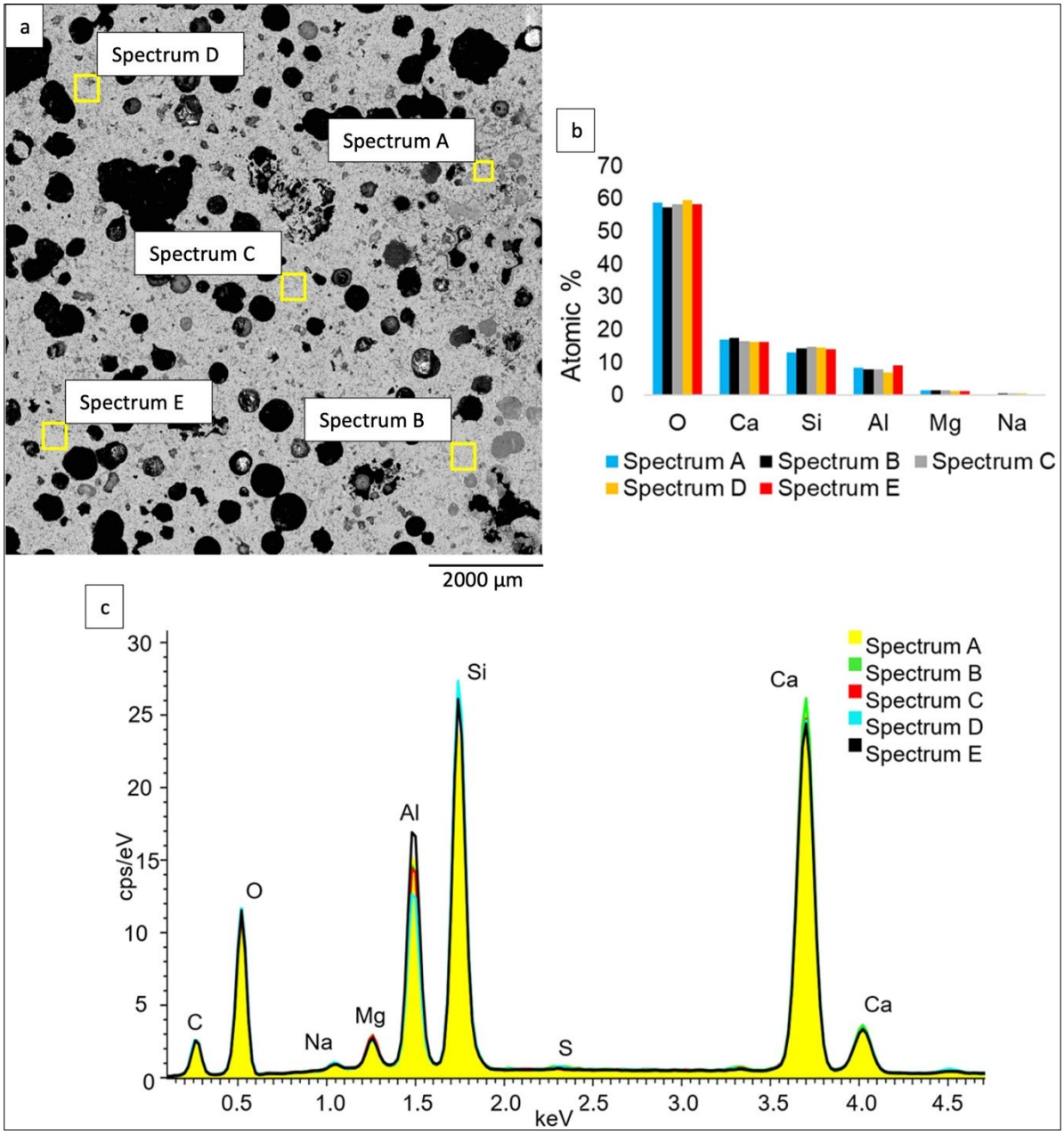

Fig. S12. Comparison of elements presence in different areas within the studied sample. (a) BSE image of the studied sample, also showing several boxed areas for which the elements atomic concentration and EDS spectra are portrayed in (b) and (c), respectively. The elements distribution is powered by the Tru-Q® feature of AZtec® flex.

S7. Variation of properties due to changes in segmentation parameters

The results of each processing pipeline represent the base case for that particular pipeline, and they are affected by the parameters that were used in the segmentation process. To get an insight into how the calculated volume fractions and properties might be affected by the training pixels and seed points that were chosen by the user, the segmentation process was repeated using different inputs. For the TWS, we compared how changing the training pixels affects the calculated concentrations and properties, while for WS we studied how changing the parameters of the watershed wizard, by 2%, affects the calculated properties. After that, the volume fractions and properties were recalculated and were then compared to the corresponding values obtained after performing the dilation and erosion operations. Generally, applying the erosion and dilation operations results in a larger change when compared to changing the training pixels and the segmentation parameters for the TWS and WS, respectively. In Fig. S13, it is evident that applying the erosion/dilation operation results in a large change, particularly in the calculated calcite volume fraction. This is because the volume occupied by calcite is low, and any small variation caused by morphological operations will result in a large percentage change. Additionally, the presence of calcite as thin films and the complex nature of slag resulted in a large variation of volume distribution and properties after applying morphological operations.

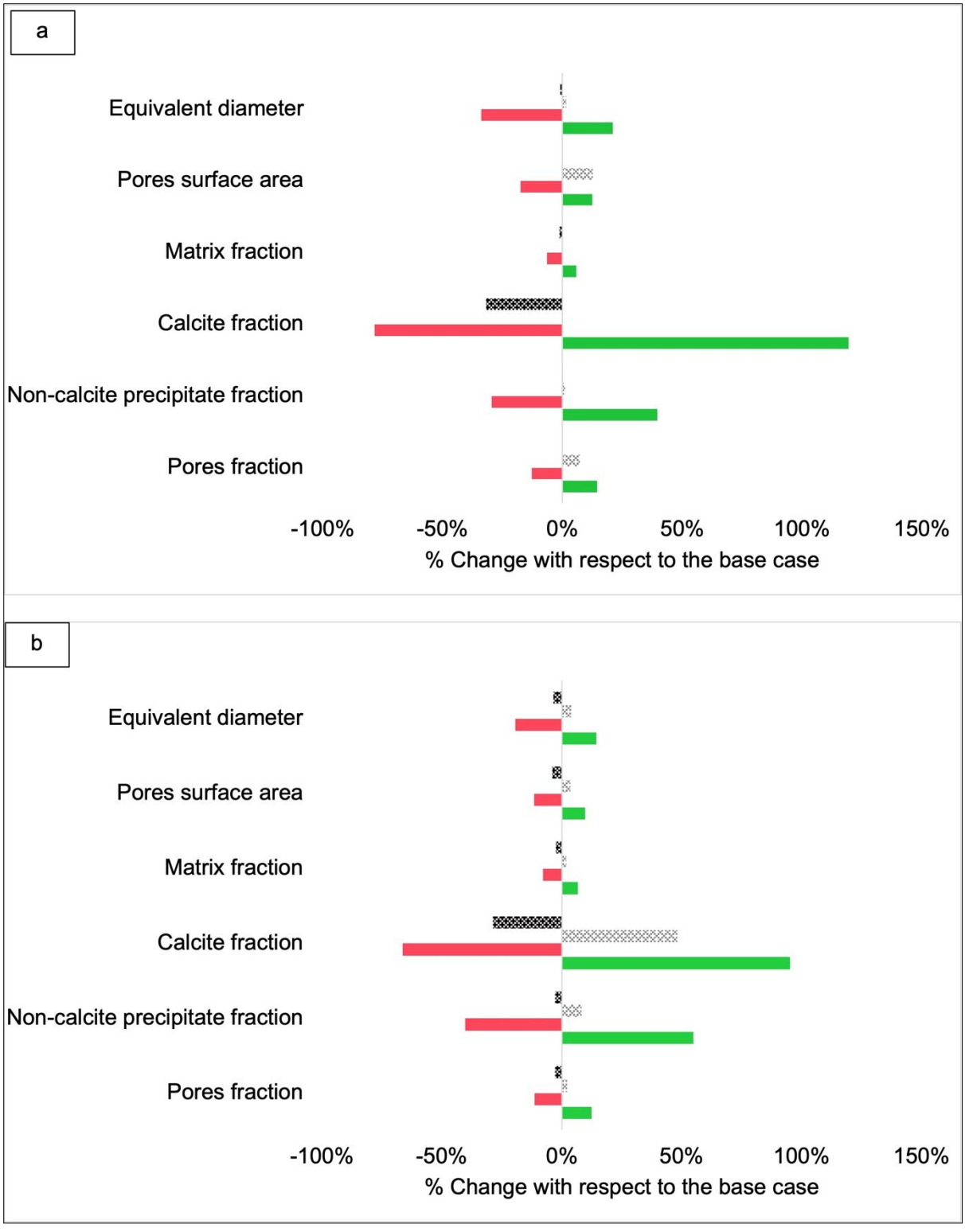

Fig. S13. Quantification of how changing the segmentation parameters affects the properties calculated based on (a) TWS and (b) WS. Red and green lines represent the deviation from the base case after applying the erosion and dilation operation to the segmentation results, while the textured grey and black lines represent the changes in the properties after changing the watershed wizard parameters by parameters by 2%.

S8. References

Arganda-Carreras, I., Kaynig, V., Rueden, C., Eliceiri, K.W., Schindelin, J., Cardona, A., Seung, H.S., 2017. Trainable Weka Segmentation: A machine learning tool for microscopy pixel classification. Bioinformatics 33, 2424–2426. https://doi.org/10.1093/bioinformatics/btx180

Arseneau, S., 2006. Structure Tensor - Tutorial and Demonstration of the uses of structure tensors in gradient representation [WWW Document]. URL https://www.cs.cmu.edu/~sarsen/structureTensorTutorial/#7 (accessed 3.17.22).

Bulgarevich, D.S., Tsukamoto, S., Kasuya, T., Demura, M., Watanabe, M., 2018. Pattern recognition with machine learning on optical microscopy images of typical metallurgical microstructures. Sci. Reports 2018 81 8, 1–8. https://doi.org/10.1038/s41598-018-20438-6

Chukwuma, J.S., Pullin, H., Renforth, P., 2021. Assessing the carbon capture capacity of South Wales' legacy iron and steel slag. Miner. Eng. 173, 107232. https://doi.org/10.1016/J.MINENG.2021.107232

Crouzet, C., Brunet, F., Montes-Hernandez, G., Recham, N., Findling, N., Ferrasse, J.H., Goffé, B., 2017. Hydrothermal valorization of steel slags-Part I: Coupled H2 production and CO2 mineral sequestration. Front. Energy Res. 5, 1–12. https://doi.org/10.3389/fenrg.2017.00029

Kriskova, L., Pontikes, Y., Pandelaers, L., Cizer, Ö., Jones, P.T., Van Balen, K., Blanpain, B., 2013. Effect of High Cooling Rates on the Mineralogy and Hydraulic Properties of Stainless Steel Slags. Metall. Mater. Trans. B 2013 445 44, 1173–1184. https://doi.org/10.1007/S11663-013-9894-9

Latham, S.J., Varslot, T., Sheppard, A., 2008. Automated registration for augmenting micro-CT 3D images. ANZIAM J. 50, 534. https://doi.org/10.21914/anziamj.v50i0.1389

Mathworks, 2022. 2-D correlation coefficient - MATLAB corr2 [WWW Document]. URL https://uk.mathworks.com/help/images/ref/corr2.html (accessed 3.23.22).

Pan, S.Y., Chang, E.E., Kim, H., Chen, Y.H., Chiang, P.C., 2016. Validating carbonation parameters of alkaline solid wastes via integrated thermal analyses: Principles and applications. J. Hazard. Mater. 307, 253–262. https://doi.org/10.1016/J.JHAZMAT.2015.12.065

Preim, B., Botha, C., 2014. Image Analysis for Medical Visualization, in: Visual Computing for Medicine. Morgan Kaufmann, pp. 111–175. https://doi.org/10.1016/B978-0-12-415873-3.00004-3

Purswani, P., Karpyn, Z.T., Enab, K., Xue, Y., Huang, X., 2020. Evaluation of image segmentation techniques for image-based rock property estimation. J. Pet. Sci. Eng. 195, 107890. https://doi.org/10.1016/j.petrol.2020.107890

Weickert, J., 1999. Coherence-Enhancing Diffusion Filtering. Int. J. Comput. Vis. 31, 111–127.